# Simulations and experimental tests for preparing the muCool 2024 beamtime

## Master Thesis in Physics

**Andrej Isaac Maraffio**

Supervised by

Prof. Dr. Aldo Antognini
Prof. Dr. Lea Caminada
Giuseppe Lospalluto

May 2025

I, Andrej Isaac Maraffio, declare that this thesis titled, 'Simulations and experimental tests for preparing the muCool 2024 beamtime' and the work presented in it are my own. I confirm that:

- This work was done wholly or mainly while in candidature for a research degree at this University.

- Where any part of this thesis has previously been submitted for a degree or any other qualification at this University or any other institution, this has been clearly stated.

- Where I have consulted the published work of others, this is always clearly attributed.

- Where I have quoted from the work of others, the source is always given. With the exception of such quotations, this thesis is entirely my own work.

- I have acknowledged all main sources of help.

- Where the thesis is based on work done by myself jointly with others, I have made clear exactly what was done by others and what I have contributed myself.

Signed:

_____

Date:

_____

*"Ci sono soltanto due possibili conclusioni: se il risultato conferma l'ipotesi, allora hai appena fatto una misura. Se il risultato è contrario alle ipotesi, allora hai fatto una scoperta."*

- Enrico Fermi

# *Abstract*

At the Paul Scherrer Institute (PSI), the muCool experiment aims to produce a device that compresses the phase space of a positive muon beam by a factor of $10^9$ with up to $10^{-4}$ efficiency. This device consists of a helium gas target that operates at cryogenic temperatures, featuring a vertical temperature gradient and complex electric and magnetic fields. After compression, the cooled muon beam is extracted into vacuum through a windowless orifice and re-accelerated to keV energy levels for use in precision experiments.

This thesis focuses on the preparation steps to test the muon extraction stage. A series of experiments and simulations were conducted to solve crucial difficulties. To deal with heat control, various cooling methods were tested to determine the possibility for installation. For electrical stability, breakdown voltage tests were conducted to check whether the optimal electrical field could be applied in practice. Furthermore, simulations were performed to determine the optimal positioning of scintillators that expose the muon motion, complemented by measurements on how to effectively couple scintillators to SiPMs.

During the beamtime in 2024, a target designed for compression and extraction from the orifice was tested for the first time. This marked a significant step toward achieving the full operation of the muCool device.

# Acknowledgements

First of all, I'd like to express my sincere thanks to Prof. Dr. Lea Caminada for allowing me to complete my master's thesis under her supervision.

I am extremely thankful to Prof. Dr. Aldo Antognini for allowing me to join his group for this project. Working under the pressure of a coming soon beamtime gave me an unique and intense experience. Being part of that challenging yet gratifying period was both a challenge and a privilege.

A particular thanks to my supervisor and friend, Giuseppe Lospalluto, who supported me throughout the entire process. He assisted me in navigating the hurdles I encountered and encouraged me to find innovative solutions to the problems that arose during my thesis work.

I would also like to thank Ivan Solovyev, who helped me with the GEANT4 simulations. His expertise and assistance were essential to the success of my project.

I am also grateful to all members of the muCool collaboration, who's support and friendship made this challenging time special.

Thank you to my girlfriend, Amélie Jampen, for always patiently listening to my explanations of my master project and supporting me when I prepared my presentation.

A particular thank you to my parents, Mamma and Bapo, for their continuous support during my studies. Thank you for always being there for me, in both good and difficult times. I am extremely thankful to my father, Bapo, who was a study buddy throughout my bachelor's and master's degrees. Your guidance in exam preparation, as well as your persistent encouragement, contributed significantly to my success.

Thank you everyone for your encouragement, motivation, and faith in me.

# Contents

# Introduction

The muon ($\mu$) is a lepton of the second generation, with a mass of 105.7 MeV/c$^2$. The muon is unstable and has a lifetime of 2.2 µs, however, this is long enough to carry out a variety of experiments. These experiments are essential to perform precision measurements to verify Standard Model predictions.

Due to parity violation in the weak interaction, muon beams are always polarised. Precision experiments, including searches for the muon electric dipole moment, measurements of the anomalous muon magnetic moment (g-2), and studies of charged lepton flavour violation in forbidden decays, are made possible by these beams [1]. Additionally, in solid-state physics, muons are used to measure materials magnetic properties through the muon spin rotation (µSR) technique [2]. Muons ($\mu^+$) and electron can form muonium, a bound state combining a positive muon and an electron. The absence of hadrons in this state makes it interesting for accurate testing of quantum electrodynamics (QED). Transitions between the 1S and 2S states in muonium can be measured by spectroscopy, which offers an accurate test of QED and makes it possible to calculate fundamental constants like the muon electron mass ratio [1] .

To conduct these experiments, high-quality, low-energy muon beams are essential. However, only a few facilities can produce such beams, including TRIUMF, J-PARC, and the Paul Scherrer Institute (PSI). At PSI, a high-power 1.3 MW cyclotron generates a 590 MeV proton beam that strikes a graphite target, causing proton-proton interactions that produce pions ($\pi$). Through the weak interaction, pions decay into muons and neutrinos, as represented by the following reaction:

$$\pi^+ \rightarrow \mu^+ + \nu_\mu \quad . \tag{1}$$

Since this decay is a two-body process, all muons produced from the decay of the pion at rest have 4 MeV energy, corresponding to a momentum of 28 MeV/c. In addition, the neutrinos are left-handed, meaning that the resulting positive muons are right-handed.

The muons produced can be categorized into three types:

- *Surface Muons*: These monochromatic muons have a momentum of 29.8 MeV/c and are produced when pions decay close to the target's surface.

- *Subsurface Muons*: These muons, which have momenta between 10 and 29.8 MeV/c, are created when pions decay inside the target.

- *Cloud muons*: These muons have a wide variety of momenta and are produced when pions decay outside the graphite target while in flight.

In the high-intensity frontier, where high statistics is required, surface muons are typically used for experiments. On the other hand, a slow muon beam of sufficient intensity but with a much smaller phase space (transverse size, momentum spread, and divergence) would be extremely useful for various other particle physics studies. Producing slow muon beams with moderate energy out of surface muons is not simple; the muon lifetime is only 2.2 $\mu s$, which means that conventional cooling methods like electron cooling and stochastic cooling cannot be used.

To achieve this, a novel cooling method is required, which is the focus of the muCool experiment: it consists of a cryogenic helium gas target, positioned in a 5 T magnetic field. A surface muon beam is stopped in the helium gas, which reduces the muon energy from few MeV to several eV. The "stopped" muon cloud is then manipulated by using complex electric and magnetic fields and gas density gradients. The muons are then extracted from the gas into vacuum, through a windowless orifice, re-accelerated to keV energy via a static or pulsed electric field, and then extracted from the magnetic field. muCool reduces the phase space of a surface muon beam by a factor of $10^9$ with up to a compression efficiency of $10^{-4}$, which is in part limited by the short muon lifetime [3].

My contribution to this experiment involved the development of a target designed to extract muons from the muCool target into the vacuum, which was first tested during the beamtime of 2024.

This thesis presents the simulations and experimental tests conducted in preparation for this new target. It includes heat transfer simulations, experimental investigations of the electrical stability of the target, and simulations for detecting the motion of the muons.

# Chapter 1

# muCool: Dynamics and Compression of Muons in Helium

The muCool experiment is based on a phase space compression scheme that relies on interactions between positive muons and helium gas in the presence of strong electric and magnetic fields. It is necessary to study these interactions to fully understand the muon motion in the mucool target.

This chapter presents an analysis of muon motion in E and B-fields firstly in vacuum and later examining their dynamics in the gas environment. It goes through essential stages, beginning with an understanding of the interaction processes and concluding with experimental confirmation of compression techniques. These include transverse compression, longitudinal compression, and mixed transverse-longitudinal compression.

## 1.1   Muon-Helium Physical Processes

In the muCool experiment muons from a few MeV energy are cooled down to 1-10 eV. In this cooling process the muons are not only decelerated, the beam phase space is also reduced. During this process, the interactions that muons and helium gas atoms undergo are the following:

- From few MeV to keV: Muons lose energy mainly through helium ionisation and excitation.
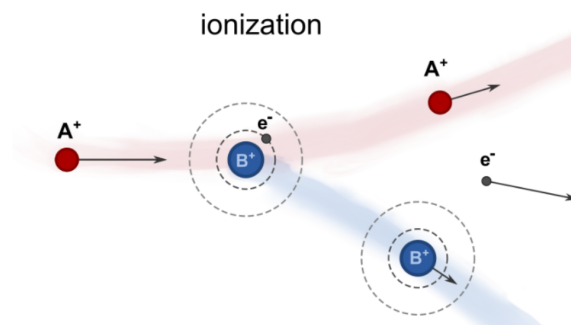
Figure 1.1: A$^+$ (muon) ejects an electron, ionizing B (neutral He gas atom). Taken from [4].
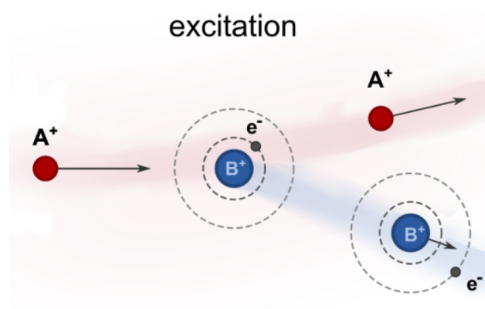


Figure 1.2: A$^+$ (muon) transfers energy, exciting B (neutral He gas atom). Taken from [4].

- From keV to 100 eV: Most of the energy is lost during charge exchange reactions, which result in the formation and ionisation of muonium (Mu).
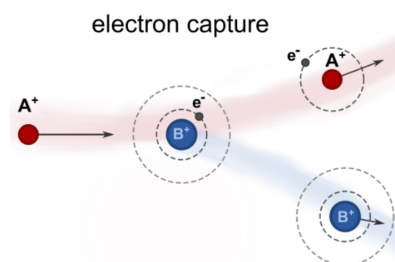


Figure 1.3: A$^+$ (muon) captures an electron from B (neutral He gas atom) forming muonium. Taken from [4].

During the creation process, muonium with a binding energy of 13.6 eV is produced $\left(\mu^+ + \text{He} \rightarrow \text{Mu} + \text{He}^+\right)$.

The ionisation process occurs when the muonium collides with a helium atom and loses its electron, setting the muon free once more $(\text{Mu} + \text{He} \rightarrow \mu^+ + \text{He} + \text{e}^-)$.

In this energy range, a single muon can go through several cycles of ionisation and muonium production while slowing down [4].

- From 100 eV to eV: Muons lose energy mostly through elastic interactions.
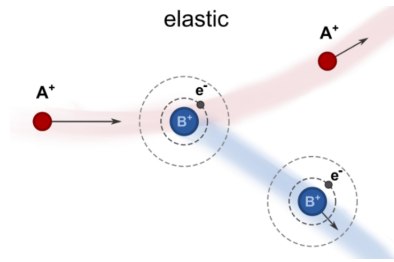
Figure 1.4: A$^+$ (muon) deflects off B (neutral He gas atom) with no change to B's internal state. Taken from [4].

## 1.2 Muon motion in the muCool target

Figure 1.5 illustrates the original muCool scheme [5]. Muons of a few MeV energy enter a cryogenic helium gas target within a 5 T magnetic field and are decelerated to 1-10 eV. Let us analyse the different compression stages separately.
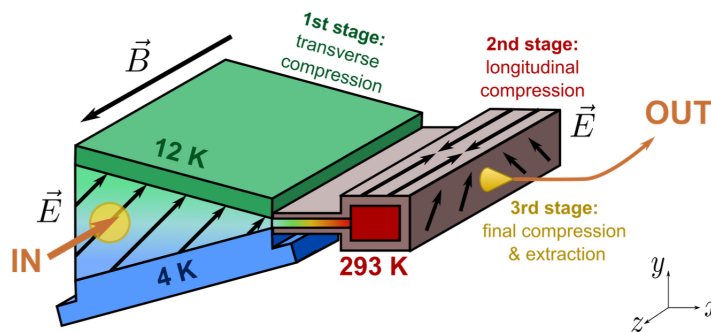


Figure 1.5: A surface muon beam is stopped in cryogenic helium gas within a 5 T magnetic field and then compressed in various stages using the magnetic field, electric fields and density gradients. The muon "swarm" experiences transverse, longitudinal, and final compression before it is extracted into a vacuum and re-accelerated for further experiments. Taken from [6].

### 1.2.1 Transverse Compression Stage

During the transverse compression stage, muons with energy of several eV drift in the +x-direction, while being compressed in the y-direction.

To demonstrate this first compression stage, the E-field was arranged at a $45\,\text{deg}$ angle with respect to the x-axis:

$$\mathbf{E} = \begin{pmatrix} E_x \\ E_y \\ 0 \end{pmatrix} \tag{1.1}$$

with $E_x = E_y \approx 1\mathrm{kV/cm}$.

While the B-field was orientated upstream in the $+z$ direction.

Initially, we analyze the muon motion in vacuum to understand the behavior of charged particles in a $\mathbf{E} \times \mathbf{B}$ field. In crossed $\mathbf{E}$ and $\mathbf{B}$-fields, muons experience a force along the direction of $\mathbf{E} \times \mathbf{B}$. In order to fully understand their motion, illustrated in Fig. 1.6, let's have a closer look at the trajectory of a muon that is initially at rest in these crossed $\mathbf{E}$ and $\mathbf{B}$-field, step by step:

- Muons at rest undergo only acceleration in the $\mathbf{E}$-field direction.

- Muons feel the $\mathbf{B}$-field as soon as their velocity ($v \neq 0$) increases in the direction of the $\mathbf{E}$-field.

- The $\mathbf{B}$-field deflects the muons until they travel against the $\mathbf{E}$-field and come to a stop.

- Then their motion resets and the process starts again.

There is a net movement in the $\mathbf{E} \times \mathbf{B}$ direction (in figure 1.6 the direction corresponds to the horizontal axis). This is due to the fact that the $\mathbf{B}$-field induces a force on the charged particle causing a cyclotron motion with a certain frequency.
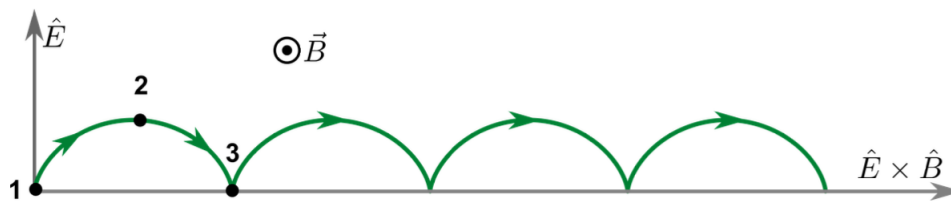


Figure 1.6: A positive muon at rest (position 1) drifts in the $\hat{E} \times \hat{B}$ direction under crossed electric and magnetic fields, following a cycloidal trajectory. Taken from [4].

Let's analyze the motion of the muons in this $\hat{E} \times \hat{B}$ field in the helium gas. The muCool target's conditions lead to muon-helium interactions with an average frequency of $\nu_c$. The collision frequency can be shown to depend on N, the number of density of helium gas, $v_r$, the relative velocity, and $\sigma_{EL}(v_r)$, the cross section for elastic collisions [4].

$$\nu_c = N \sigma_{EL}(v_\mathrm{r}) v_\mathrm{r} \quad . \tag{1.2}$$

As illustrated in Fig. 1.7, this frequency influences how the muon moves in the crossed E and B-fields. It gives rise to a deflection angle $\theta$ with respect to the $\hat{E} \times \hat{B}$ direction. The deflection angle can be derived from the ratio of the velocities in the given directions resulting in the ratio of the collision frequency and the cyclotron frequency [5].

$$\tan\theta = \frac{\bar{y}'}{\bar{x}'} = \frac{\nu_c}{\omega}. \tag{1.3}$$

The deflection angle increases for high collision frequencies, compared to the cyclotron frequency, and is smaller for low collision frequencies, as seen in Fig. 1.7.
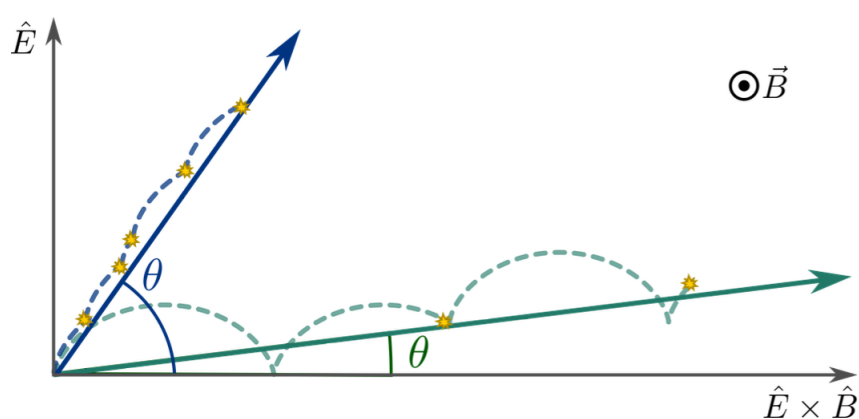


Figure 1.7: Muons at rest drift under crossed electric and magnetic fields, following interrupted cycloidal motion due to collisions with helium atoms (yellow stars). Collisions deflect the drift direction from the $\hat{E} \times \hat{B}$ direction by an angle $\theta$, with higher collision frequencies, resulting in larger deflection at higher gas densities (blue) and lower collision frequencies, resulting in smaller deflection at lower gas densities (green). Taken from [4].

This shows that adjusting these variables allows us to modify the trajectory of the muons. By creating a vertical temperature gradient, as in Fig. 1.5, the density of helium in the target varies at different points, allowing us to compress the muons in the y- direction.

## 1.2.2   Longitudinal Compression Stage

After transverse compression, muons are guided to the room-temperature longitudinal compression stage to reduce the z-direction muon "swarm" size. At this step, an electric field of the type:

$$E = \begin{pmatrix} 0 \\ E_y \\ -E_z \cdot \frac{z}{|z|} \end{pmatrix}$$

is applied within the gas, with $E_y = 2 \cdot E_z \approx 1$ kV/cm. This electric field contains a component ($E_y$) perpendicular to the magnetic field and a component parallel to it, pointing towards the centre of the target at z = 0. Since the electric field is parallel to the magnetic field, the muon drift velocity points longitudinally in the z-direction towards the target centre. At low density, the perpendicular electric field component ($E_y$) causes drift velocity to have a component in the $\hat{E} \times \hat{B}$ direction, which corresponds to the +x-direction. Thus, muons are compressed in the z-direction and transferred to the final stage with extraction into vacuum (Fig. 1.5).

### 1.2.3 Mixed transverse-longitudinal compression

The muCool longitudinal and transverse compression stages were separately demonstrated [6]. Next these two stages were combined into the transverse-longitudinal compression phase, which compresses transversely and longitudinally in one step. Figure 1.8 shows how the mixed compression target uses complex electric fields to achieve transverse and longitudinal compression at cryogenic temperatures with a temperature gradient.
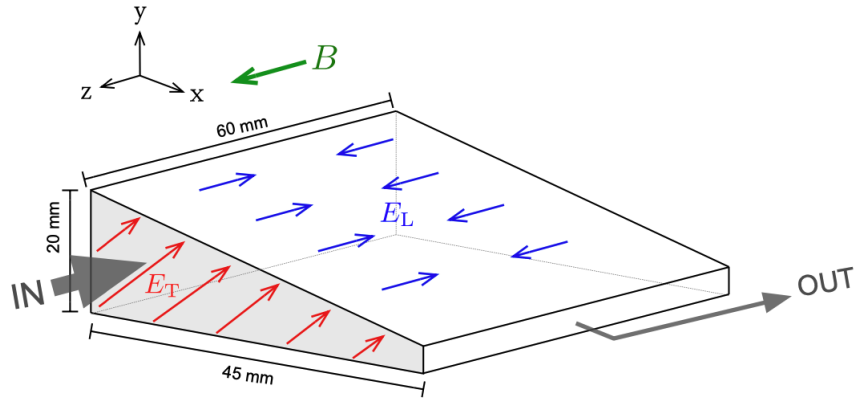


Figure 1.8: The working principle of mixed transverse-longitudinal compression includes stopping of muons inside a helium gas volume kept at cryogenic temperatures, characterised by a temperature gradient. The magnetic field in combination with an electric field with both transverse ($E_T$) and longitudinal ($E_L$) orientation is used to control particle motion. Taken from [7].

The drift velocity of the muons can be determined by taking into account the presence of electric (E) and magnetic (B) fields, as well as gas collisions as follows:

$$\vec{v}_D = \frac{\tilde{\mu} E}{1 + \omega^2/\nu_c^2} \left[ \hat{E} + \frac{\omega}{\nu_c} \hat{E} \times \hat{B} + \frac{\omega^2}{\nu_c^2} (\hat{E} \cdot \hat{B}) \hat{B} \right] \tag{1.4}$$

with $\tilde{\mu} = e/(m_\mu \nu_c)$ the muon mobility in the gas, $\omega = (eB)/m_\mu$ the muon cyclotron frequency with the muon mass $m_\mu$ and $\nu_c$ the average collision frequency of the muon with helium gas atoms.

As muons move in the $+x$ direction, their spatial dispersion shrinks. The transverse electric field component $(E_T)$ compresses the y-distribution, whereas the longitudinal component compresses the z-distribution. The development of the mixed compression target is technically challenging. This target requires a stronger electric field than longitudinal and transverse compression targets. To efficiently guide muons through the gas, the mixed compression target requires a total electric field intensity of up to 1.5 kV/cm.

### 1.2.4 Mixed compression with extraction

Mixed compression in a closed target was demonstrated during beamtime 2019 [7]. The primary goal of beamtime 2024 is to extract muons from the target into the vacuum, which is also the most challenging step for the muCool experiment.
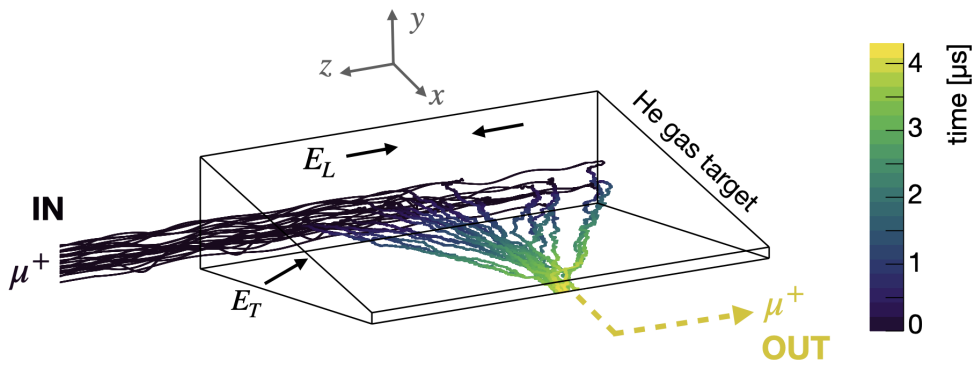


Figure 1.9: Illustration of the mixed compression target embedded in a 5T magnetic field, with a cryogenic temperature gradient and electric field components ($E_L$ and $E_T$). Muon trajectories, simulated with GEANT4, shows the compression process, with the colour scale representing the time from entering the target. Taken from [3].

This implies that after the phase space compression, muons approach the tip of the target and are extracted through a tiny windowless orifice, as illustrated in Fig. 1.9 - 1.10. Maintaining a consistent gas pressure and keeping the density gradient inside the target is challenging, since helium gas constantly escapes through the orifice.
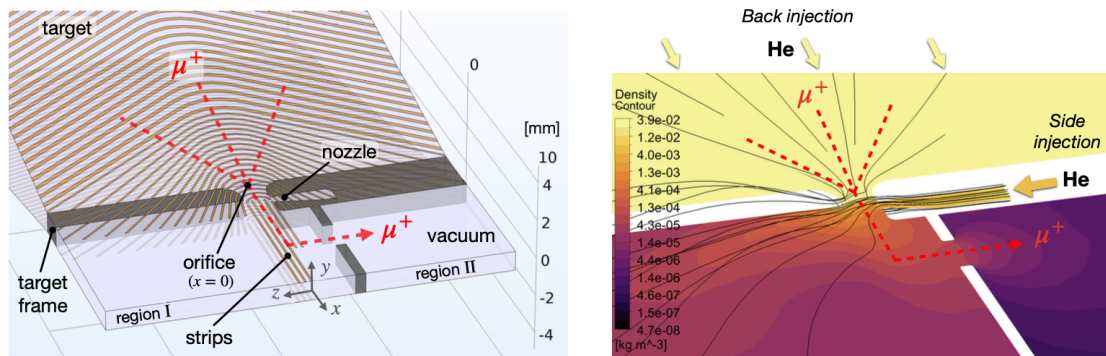


Figure 1.10: (Left) Schematic of the extraction stage: The orange electrodes provide the electric field to steer the muons, while the grey plastic frame defines the orifice channel and two differentially pumped areas (Region I and Region II). (Right) Density contours of helium gas at the orifice region, simulated using ANSYS, with black lines indicating velocity streamlines [3].

A sophisticated helium gas circuit was therefore designed. The system consists of two gas injections: a "back injection" to maintain constant pressure in the target and "a side injection" to produce a gas barrier near the aperture, as shown in Fig. 1.10.

# Chapter 2

# muCool Target

During beamtime 2024, a target designed for mixed compression and extraction from an orifice was tested for the first time. This marked a significant step toward achieving the full operational ability of the muCool experiment. All tests mentioned in the following chapters occurred under similar conditions to those expected during beamtime.

The experimental setup includes a solenoid magnet that generates a 5 Tesla magnetic field. The target is precisely positioned at the centre of the solenoid. To provide the necessary temperature gradient, the target is cooled at the bottom and heated at the top. A Pulse Tube Cryocooler is used to cool to a temperature of 6K a copper finger that serves as both the support for the muCool target and the thermal link to generate the temperature gradient in the target. This chapter describes the target's design and functionality.

The target is made of a 3D-printed plastic frame around which a flexible PCB (Printed Circuit Board) is wrapped and glued with stycast epoxy resin as shown in Fig. 2.1. The PCB consists of a Kapton foil with printed copper traces that generate the required electric field. Sapphire plates are attached to the top and bottom of the Kapton foil in order to regulate the temperature. However, the materials' dissimilar thermal contractions provide an important challenge: when cooled to cryogenic temperatures, plastic contracts significantly more than sapphire. This issue is addressed in Chapter 3.
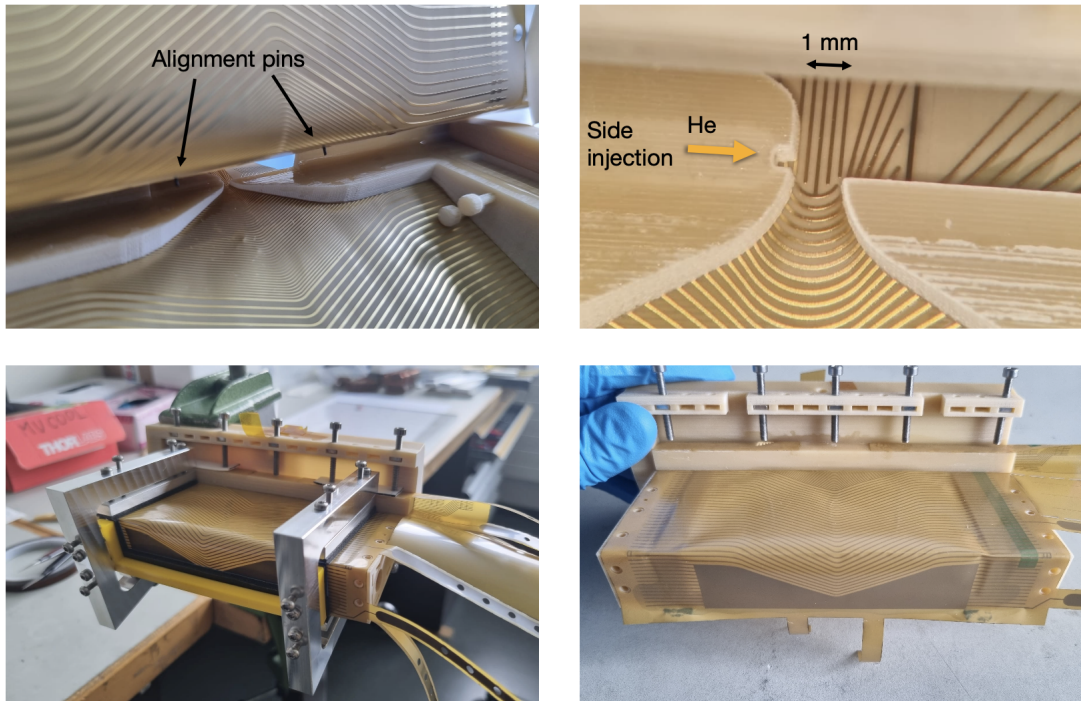
Figure 2.1: (Top Left) Image of the target during the glueing process. (Top Right) A picture of the orifice area showing the precise alignment obtained in the positioning of the strip electrodes relative the target frame. (Bottom Left) Photograph of the target during the glueing process, showing the applied support and pressing mechanisms. (Bottom Right) Picture of the glued target without any sapphires.

To achieve optimal target performance, the temperature gradient has to be stable from the target's back to the orifice. This creates additional complications at the orifice, where the aperture of 1 mm (y) x 1.3 mm (z) is defined by the 3D printed plastic.

The target's functioning depends heavily on:

- *Precise heat and temperature control*

- *Electrical stability*

- *Detection of positrons.*

Each of these aspects needs major testing to ensure precise measurements during the experiment.

Efficient cooling at the target's bottom and heating at the top are critical for maintaining the desired temperature gradient. Sapphire plates attached to the Kapton foil maintain the gradient in the target's central region. However, overcoming the orifice region's cooling issues, due to the thermal contraction mismatch between the plastic and other materials, required new methods.

Experiments using plastic bars, in particular L-shaped bars, were carried out to improve cooling and heating in this region, as described in Chapter 3.

Applying high voltage to the target electrodes is required to produce the strong electric field needed to steer muons inside the target. Electrical breakdown tests were performed in order to ensure that the system could withstand these conditions. On top of that, during the experiment, free charges moving in the target (such as electrons or He ions, see Chapter 1) could accumulate on the plastic's dielectric surface, resulting in stray electric fields. To prevent this, the plastic surface must have a non-zero conductance so that charges could dissipate. In search of suitable solutions, tests were conducted involving materials such as aluminium pyro MT, graphite, aluminium powder, and Electrostatic Dissipative (ESD) coatings (both liquid and aerosol). These tests are outlined in Chapter 4.

To expose the muon motion inside the target, positrons generated from their decay are detected by scintillators placed outside the target. To observe phase space compression and extraction, these detectors needed to be precisely placed within a copper collimator. However, due to the target's 3D-printed plastic design at the extraction region, copper collimation could not be used, requiring alternate ways for reducing false signals. To fix this, the scintillators were placed in specially constructed 3D-printed holders. Simulations and positional optimization of the detectors and holders were conducted to ensure reliable performance. These are summarised in Chapter 5.

The tests demonstrated the target's readiness to function for temperature control, electrical stability, and positron detection. These efforts ensure that the muCool experiment's operation is stable and that muon compression and extraction stage can be experimentally tested.

# Chapter 3

# Heat and Temperature control

Thermal management is essential for the muCool experiment: the working principle of the muCool device is based on maintaining a temperature gradient over the full target. The biggest challenge was maintaining a temperature gradient in the orifice region. Here the plastic frame defines the physical aperture through which muons are extracted and plastic bars are used to align the kapton foil to the frame.

To ensure the temperature gradient at the orifice region, the plastic bars need to be maintained at the correct temperatures. Figure 3.1 presents an ANSYS simulation of the system, showing the temperature distribution throughout the target. Here cylindrical copper rods are inserted in the plastic bars and cooling of the rods in turn cools the plastic bars. The results showed that while the lower bar may be efficiently cooled, the upper bar tended to experience heating from thermal radiation and other heat sources. Cooling the lower bar is crucial for preserving the temperature gradient required for good performance. Additional improvements to the cooling system are necessary to maintain the inside target temperature within the specified range of 6.5 K to 22 K.

This chapter addresses methods to satisfy the cooling requirements of the plastic bars, optimising thermal connection between materials, while also considering problems related to material compatibility and structural integrity. To get initial insights into the cooling of plastic bars, a number of simulations and tests were conducted with a simpler setup. This consists of copper bar, a plastic bar and a heating source to reproduce the real experimental conditions.

First, we present thermal simulations of this simple setup performed with COMSOL Multiphysics. Then we summarise the experimental tests carried out at cryogenic temperatures to verify the simulation results. These studies were essential to understand the thermal requirements of the muCool apparatus and gradually directed the design towards a new cooling system.
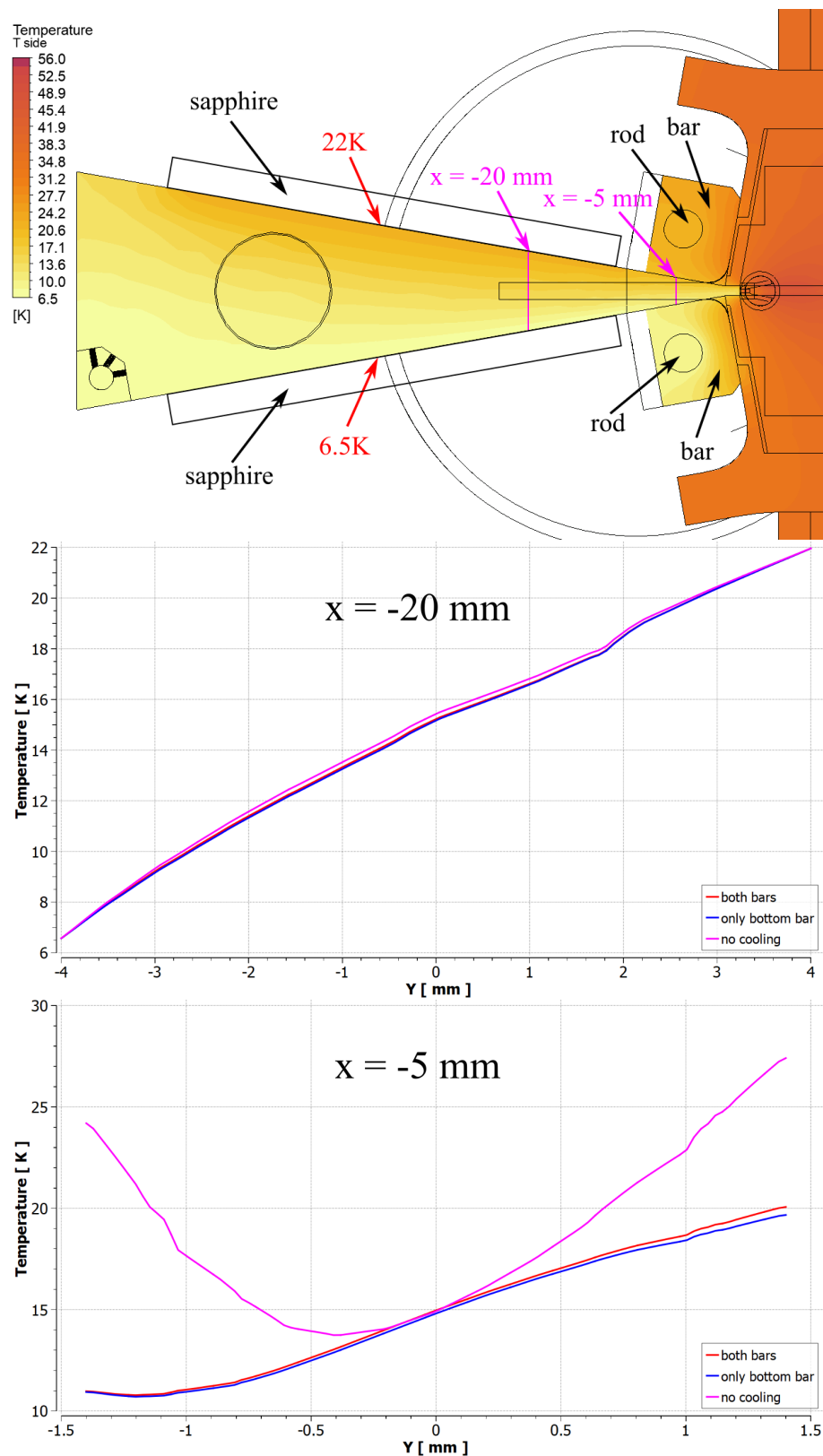
Figure 3.1: (Top) Target temperature distribution at z = 0, with two purple lines indicating the positions where temperature was analyzed along the specified axis.
(Middle) Temperature variation along the left purple line at x = -20 mm, comparing 3 cases: no cooling, cooling with only bottom bar, cooling with both bars [8].
(Bottom) Temperature variation along the right purple line at x = -5 mm for the same cases as above [8].

## 3.1  Heat Transfer Simulations with COMSOL

### 3.1.1  COMSOL Multiphysics

COMSOL Multiphysics is a flexible finite element method (FEM) [9] software which is able to simulate complicated multiphysics problems such as heat transport, fluid dynamics, and electromagnetism, in a unified manner. Its key features include:

- **Geometry Definition:** Users can design or import models representing the physical components of the system.

- **Material Assignment:** Provides a framework for defining material properties such as thermal conductivity and specific heat.

- **Boundary Condition Setup:** Helps defining interactions with the surrounding environment, such as heat flux or temperature constraints.

- **Mesh Generation:** Creates a fine-tuned meshed/grid to ensure accurate calculations while maintaining computational efficiency.

- **Simulation Execution and Analysis:** Solves governing equations and visualizes results for interpretation.

### 3.1.2  Simulation Setup

The simulation technique involved:

1. **Defining Geometry:** The model represented a 1 cm × 1 cm × 10 cm L-shaped "Visijet" plastic bar [10]. The plastic bar was connected to a copper bar using a connecting medium that varied depending on the kind of connection. Extensions for a temperature sensor were added to the plastic bar, as shown in Figure 3.2.

2. **Assigning Materials:** The material properties, such as thermal conductivity and specific heat, were assigned automatically by the software based on the selected materials. For example, Visijet plastic was used for the L-shaped bar, copper for the cooling element, and different materials for the connection, as listed in point 4. The temperature dependent thermal conductivity of Visijet plastic was manually added and it is plotted in Fig. 3.3.

3. **Boundary Conditions:** The copper bar was connected to the cryostat's copper finger which was kept at 5–7 K, and the Visijet plastic was in thermal contact with the copper bar

through a thin foil of varying materials, acting as thermal connection. Heat was applied to the left wall of the L-shaped plastic bar, corresponding to the left wall seen also in Fig. 3.2.

4. **Connection Mechanisms/Materials Tested:**

   - Indium Foil (0.1 mm and 0.25 mm thickness).
   - Copper Foil (0.035mm and 0.1 mm thickness).
   - Apiezon Grease (a specialized thermal interface material).

5. **Analysis:** The simulations demonstrated the cooling efficacy of each connection type under idealised circumstances, which served to direct material selection for ideal thermal coupling.
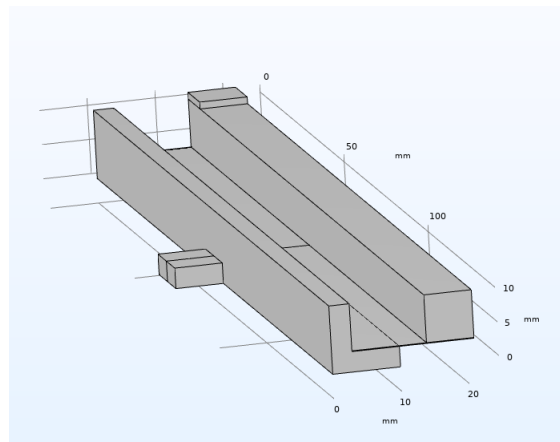


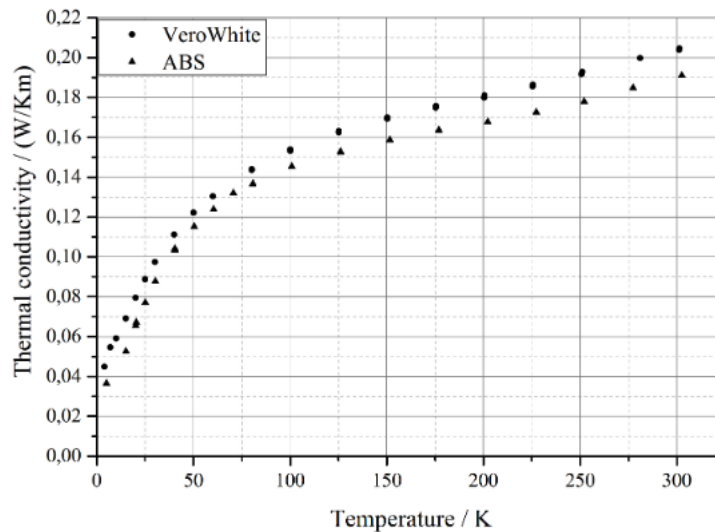Figure 3.2: L-shaped geometry used in heat transfer simulations.

Figure 3.3: VeroWhite thermal conductivity curve used in the muCool simulations (assumed to be the same as the one of VisiJet M2R-TN plastic) compared to the one of ABS, a common 3D print material [10].

The COMSOL simulations offered essential insights to improve the thermal performance of the experimental configuration. Through examination of several connection materials and arrangements, these simulations determined the optimal techniques to obtain efficient heat transmission while preserving structural integrity.

## 3.2 Cooling and Heat transfer

The experimental procedure involved connecting a copper bar to the copper finger (cooled to 6 K) and then connecting this copper bar to a plastic L-shaped bar using a variety of approaches. A heat pad was placed on the plastic bar to apply heating power during the experiment, allowing to see how effectively the different materials cooled the plastic bar. The efficacy of each connection method was assessed by heating it and observing how the system cools and reaches a steady state.

The connections were measured using several materials, including indium (0.1 mm, 0.25 mm), copper (0.1 mm, 0.035 mm) and apiezon. Each material was heated at a rate ranging from 0.1 to 1 Watt. The measurements required many days, with each data point lasting around 3-4 hours.

One important consideration during these measurements was that only a very thin layer of glue was applied, as its heat transfer properties are not well known.

The tests were conducted with the following materials and applied heat rates:
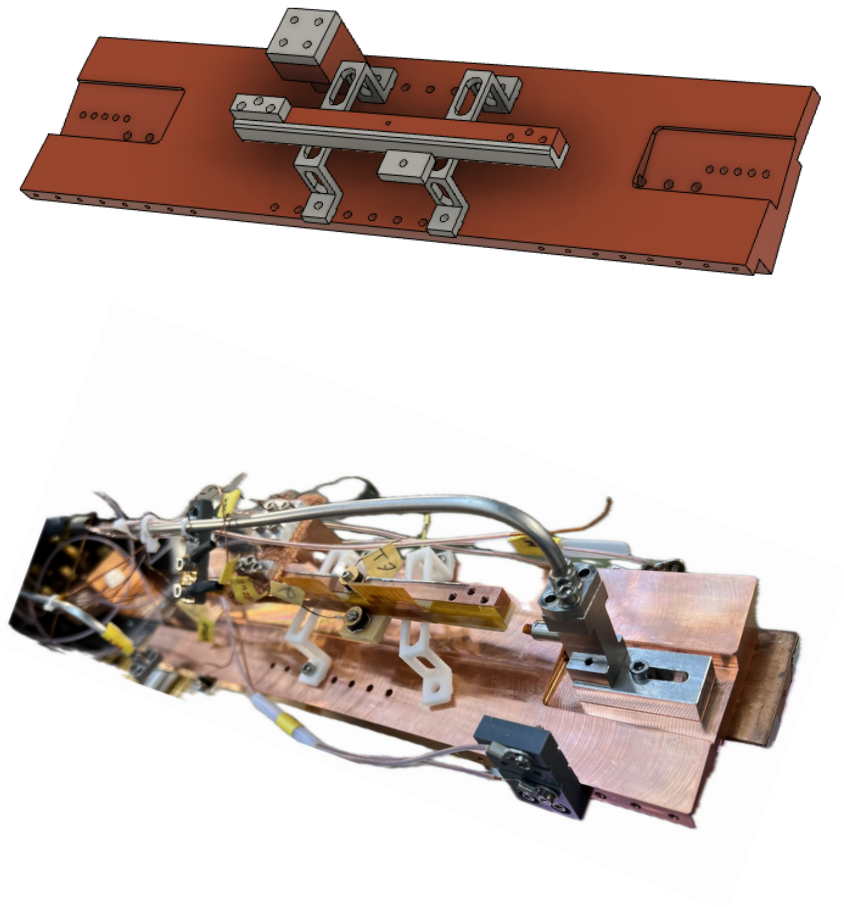
Figure 3.4: On top: Inventor setup for the plastic bar cooling tests.
Below: The actual setup mounted on the cryostat.

- Indium (0.1 mm): 0.1, 0.2, 0.5, and 0.75 Watts

- Copper (0.1 mm): 0.1, 0.5, and 0.9 Watts

- Apiezon: 0.1, 0.3, and 0.5 Watts

- Indium (0.25 mm): 0.1, 0.2, and 0.3 Watts

- Copper (0.035 mm): 0.1, 0.2, 0.3, 0.4, and 0.5 Watts

Simulations for these tests were performed using COMSOL, as described in the simulations section 3.1. These simulations provide an understanding for connecting simulated results with actual results, enabling a determination of whether the observed radiation in the experiment exceeded expectations.
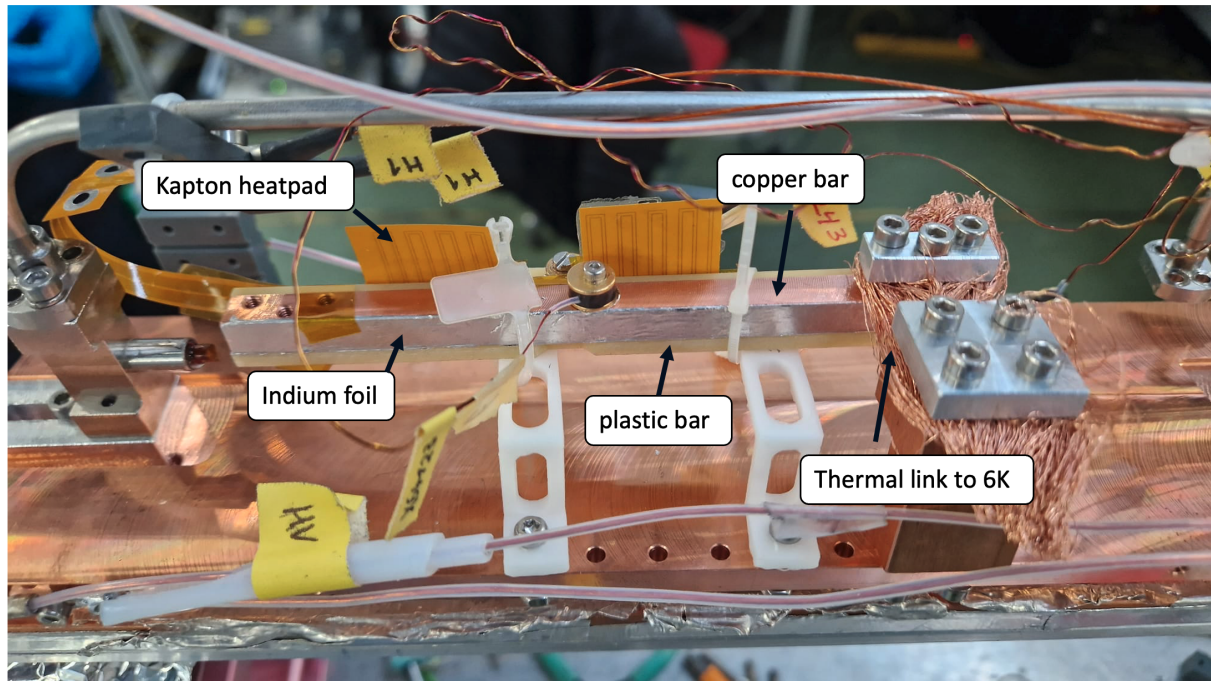
Figure 3.5: The experimental setup consists in a L-shaped plastic bar thermally connected, in this case, via an indium foil to a copper bar. The copper bar is further thermally linked to the copper finger via a thick copper braid. The configuration also includes temperature sensors and a kapton heating pad, used to provide the necessary thermal power for the tests.

## 3.3 Cooling and Heat transfer Results

This section presents the results of the performed simulations, comparing them with the experimental results for better understanding of the system's behaviour under different situations.

Figure 3.6 illustrates the experimental setup and the initial heating power used. The copper bar, coupled to the copper finger (maintained at 6 K), is shown. The indium foil, with a thickness of 0.1 mm, could not be attached, as shown in the simulation figure, due to its thinness. The copper bar was placed directly on the L-shaped plastic bar, which was glued to the indium foil to ensure an effective thermal contact. To ensure consistency when comparing experimental and simulated results, care was taken to guarantee thermal contact occurred only through the indium foil.

The same simulations and experiments were conducted with a copper foil with a thickness of 0.1 mm. The rigid structure of the experimental setup allowed for an exact replication of the simulated arrangement. Considering this stiffness, it was particularly interesting to see whether this cooling method could maintain effective thermal contact during the cooling process of the entire setup.
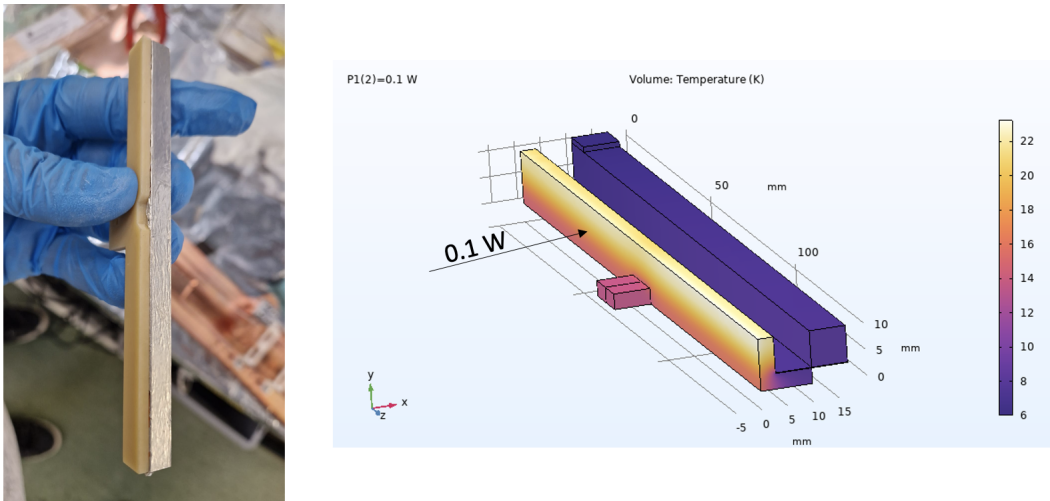
Figure 3.6: Left: Experimental configuration for cooling the plastic bar using an indium foil connection. Right: Simulations of this test with an applied heating power of 0.1 W. The colour scale indicates temperature (K).
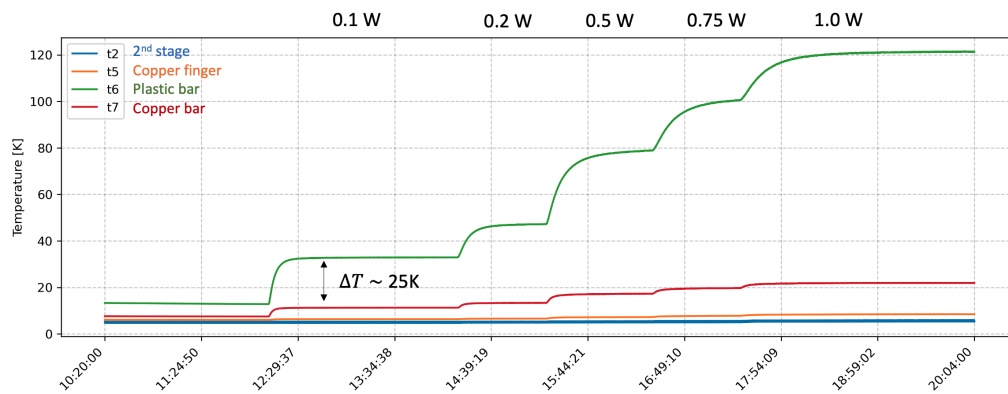


Figure 3.7: Plot of temperature versus time for the setup with indium foil of 0.1 mm. This shows how the temperature of the various elements increased for different applied power and plateaued once the system reached steady state.
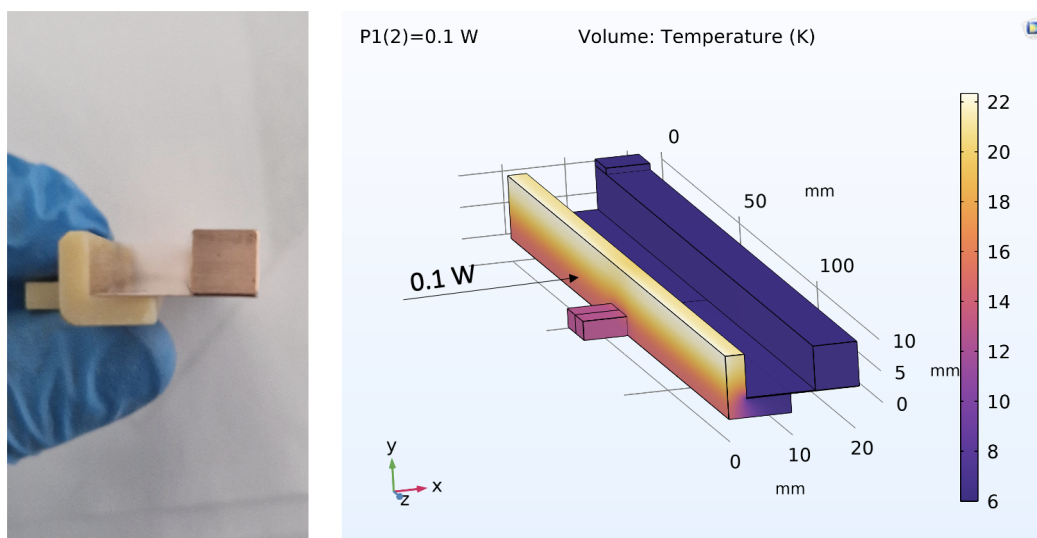


Figure 3.8: Left: Experimental setup for the plastic bar cooling with the copper (0.1 mm) connection. Right: Simulations of this test with an applied heating power of 0.1 W. The colour scale indicates temperature (K).

Following the experiment above, further simulations were necessary. After cooling, thermal contraction of the different materials resulted in the detachment of the copper foil from the plastic bar, providing thermal contact just at the edge of the copper foil. To analyze this scenario, a detached scenario was simulated to better understand its behavior.
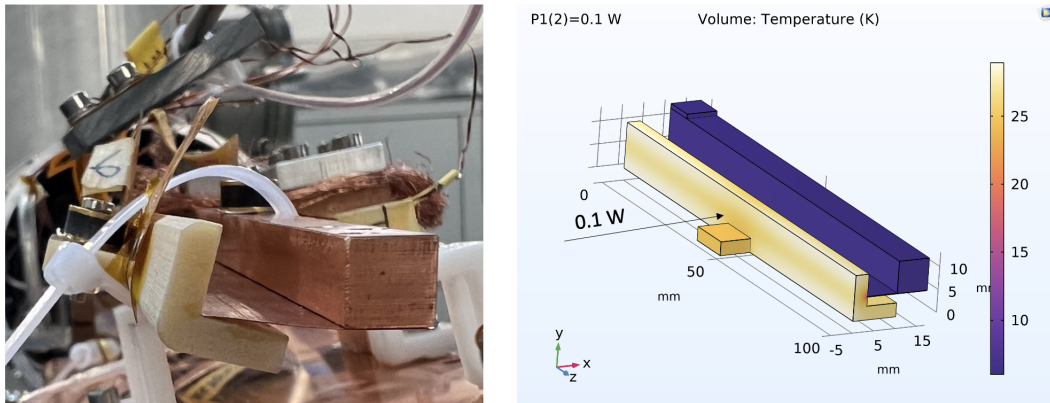


Figure 3.9: Experimental setup for the plastic bar cooling with a copper connection. During cooldown, it is likely that the plastic-copper connection detached, and simulations for this special case were performed accordingly, with an applied heating power of 0.1 W. The colour scale indicates temperature (K).

Since copper has excellent thermal conductivity, it was important to investigate whether a thinner copper connection could still provide effective cooling while being more resistant to thermal stress. Simulations and tests were done using a copper foil with a thickness of 0.035 mm 3.13. Experimental results indicated that the thin copper connection was sufficiently strong to withstand the cooling process without detaching from the plastic bar requiring cooling. Figure 3.10 illustrates that the connection was still intact after the experiment. This connection shows the potential as a cooling mechanism for the intended purpose.

Figure 3.11 compares the performance of various connections according to COMSOL simulations. As expected, the detached copper foil showed lowest levels of cooling due to its minimal contact with the surface. Similarly, Apiezon grease, despite its high thermal conductivity, shows lower efficiency compared to metallic connections. Among the metals tested, copper and indium showed similar performance, increasing their thickness resulting in increasing cooling efficiency.

Measured data is plotted in Fig. 3.12: this shows the temperature difference between the copper bar and the plastic bar as a function of applied heating power for different tested materials. When comparing simulations to experimental data (Figure 3.13), some discrepancies were observed. The Apiezon grease connection had worse performance in tests compared to the predictions made by simulations. The difference could come from insufficient thermal contact because of
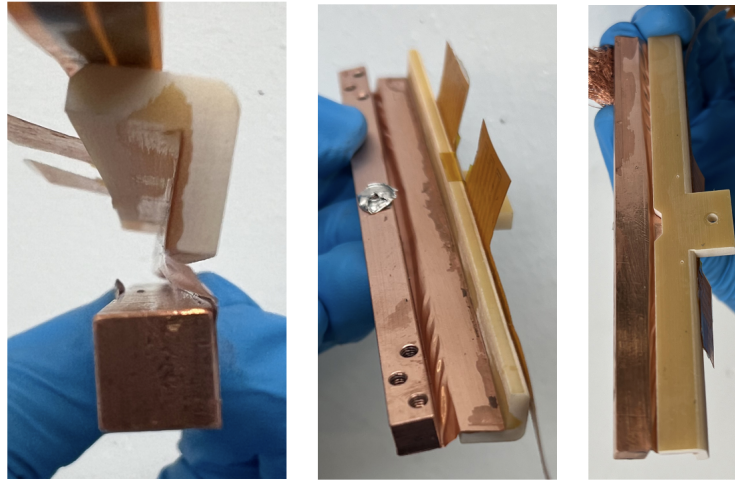
Figure 3.10: Copper cooling connection for the bar, made with a 0.035 mm thick copper foil.
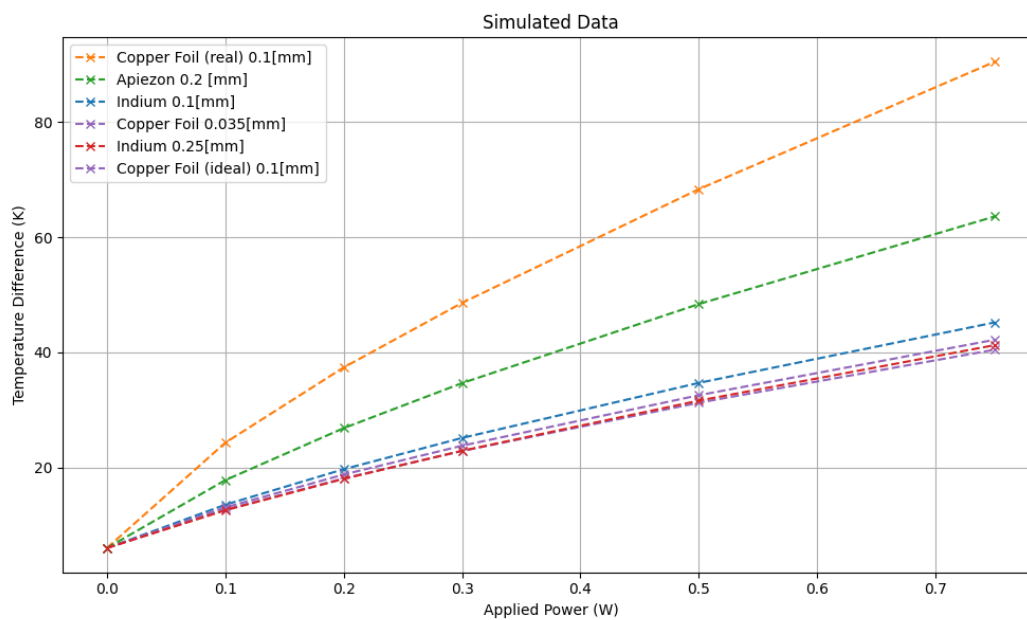


Figure 3.11: Simulated data showing the temperature difference between the copper bar and the plastic bar as a function of applied heating power for different tested materials. Two situations were simulated for the copper foil: 'Copper foil broken/real' denotes a detached situation, while 'Copper perfect' indicates an intact connection.

lack of pressure between the cooling bar and the plastic bar, together with possible changes in the setup during cooldown.

The detached copper foil simulated results were consistent with the experimental data, validating the precision of the simulations in this case. However, metallic connections revealed less successful results in tests compared to the predictions made by the simulations. This difference could be
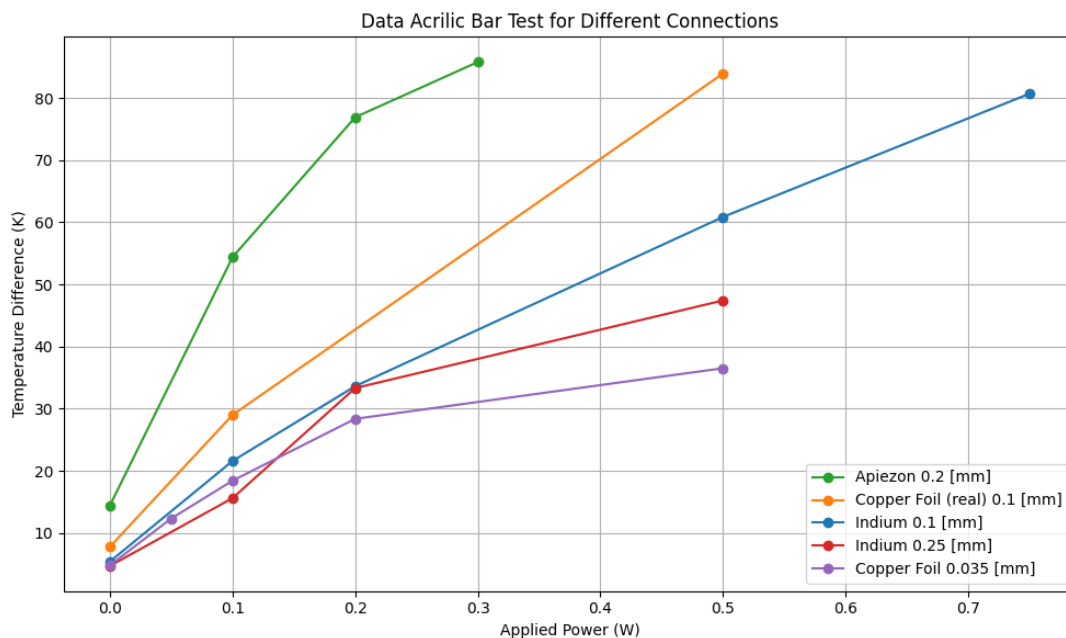
Figure 3.12: Measured data showing the temperature difference between the copper bar and the plastic bar as a function of applied heating power for different tested materials.

due to the exclusion of thermal radiation effects in the simulations, which probably significantly influence the experimental results.

The conducted tests showed that the tested alternative cooling connections are not sufficiently efficient for the requirements of the muCool experiment, as an ideal $\Delta T$ should be close to zero. These limitations, particularly not being able to solve the thermal problems at the orifice, required a complete redesign of the target bar cooling system.

To solve this challenge, the muCool collaboration performed extensive simulations to investigate alternative solutions. A potential method found was the use of helium gas for cooling the bar. The effective performance of these simulations provided one of the first reasons for the decision to redesign the target. The redesign led to the development of a target completely made of plastic cooled by helium gas. The new target design not only solved the cooling issues but also simplified the assembly and permitting to have straight copper lines at the orifice, as described in Chapter 4.

## 3.4   Conclusion

In this chapter, simulations and experiments were conducted to test alternative cooling methods of plastic bars placed close to the orifice region of the muCool target.
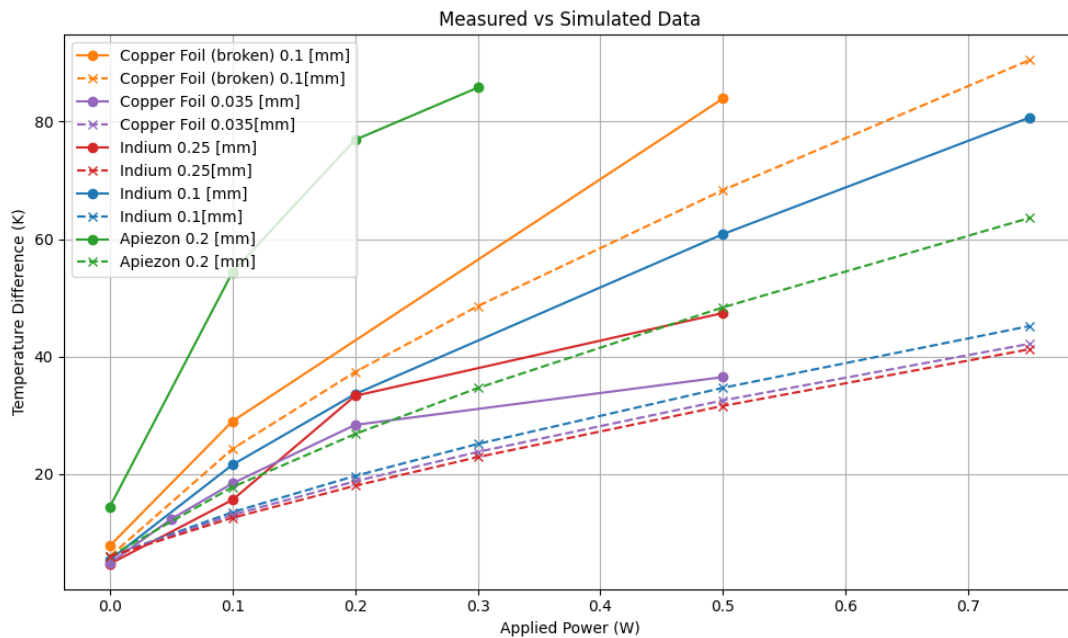
Figure 3.13: Plot showing the temperature difference between the copper bar and the plastic bar as a function of applied heating power for different tested materials for both simulated and measured data. Measured data are shown by straight lines, while simulated data are illustrated by dashed lines.

The results showed that the agreement between simulation and experiment was better for copper and indium connections compared to Apiezon. This can be related to the precise and uniform thicknesses of the copper and indium connections, which could be properly incorporated into the simulations. However, the use of Apiezon grease created larger variation between simulations and experimental results, possibly because it was impossible to precisely and consistently control the thickness of the applied layer.

The tests showed the best results were obtained with a copper connection of 0.035 mm thickness; however, even this alternative cooling connection is insufficient for the requirements of the muCool project.

The limitations found during these experiments were an important factor contributing to the redesign of the muCool target. The new design is a fully plastic target cooled by helium gas, providing a more efficient and reliable cooling.

# Chapter 4

# Electrical stability

## 4.1  Breakdown Voltage

An important test for the muCool experiment was to determine whether the necessary electric fields could be applied to the target under varying helium gas pressures. This implies to measure the breakdown voltage, which is the threshold voltage for stable target operation, at which electrical discharge occurs. Several tests were done for this purpose. Most of the tests were carried out with a target with sapphire plates but under similar conditions as those expected during beamtime 2024. The temperature boundaries were set by defining the temperature of the bottom sapphire at $\approx$ 7 K and the upper sapphire at $\approx$ 22 K, while changing the helium pressure. Further tests were also done with and without temperature gradient and varying the magnetic field.

In order to have a complete understanding of the target's behaviour during the voltage ramp-up, the current flow was also monitored. A Keithley Series 6400 Picoammeter was utilised to measure the current flow during the high voltage ramp-up process. A thick resistor (referred to as "Nick-Resistor") of 300 M$\Omega$, was added in series to the target, to protect the Keithley during discharge, preventing large currents flows. This safety resistor was chosen because it was promptly found and had a high resistance to limit the current to around $6000\text{V}/(300 \times 10^6 \Omega)$, which equals to $20\mu$A. This maintained the current within a safe range, avoiding damage to the Keithley.

The scheme of the setup is shown in Fig. 4.1. The voltage distribution on the target is made possible by series of resistors that act like potential dividers and creates the E-field in the target. One difference from the beamtime configuration were the electrical connections: in these

experimental settings, the electrodes of the top and the bottom of the target of Fig. 4.1 were connected together, Nick resistor was placed in series and then they were grounded.
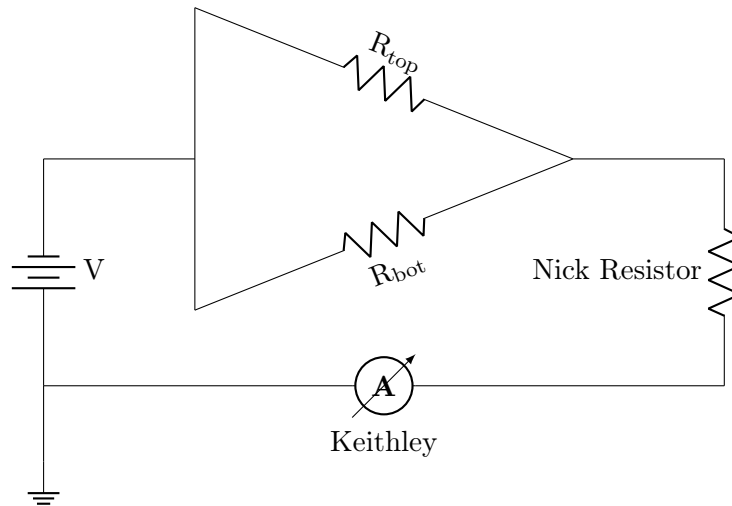


Figure 4.1: Schematic of the target's electrical system. V is the high voltage power supply. $R_{\text{top}}$ represent the resistors used for top wall, while $R_{\text{bot}}$ are the resistors applied to the copper lines bottom wall. The Nick safety Resistor is a 300 MΩ resistor to limit the current during a breakdown event. The Keithley is used as a highly precise ammeter for current measurements.

However, for the beamtime target, these electrodes were not grounded and a voltage was applied in order to guide the muons in the extraction region.

The target set up for the tests is shown in Fig. 4.2, together with the electrical connections. These experiments revealed the electrical breakdown limits of the target design.



Figure 4.2: Experimental setup for the breakdown voltage measurements. The muCool target is made of sapphire plates cooled on the bottom from the thermal contact with the copper finger and heated on the top with a Kapton heatpad. The high voltage was applied through copper wires embedded by plastic insulation.

## 4.2 Breakdown Voltage Results

As mentioned in the chapter before, the tests were performed using a power supply to ramp up the high voltage, a Keithley device to monitor the current going through the target and the 300 MΩ Nick safety resistor in series to the target. The breakdown voltage of the target was determined after calculating the effective resistance of the target. This was obtained by subtracting the Nick resistor's contribution from the total measured resistance.

The breakdown voltage tests were performed under several types of circumstances, including helium pressures of 5, 8, and 10 mbar with a temperature gradient of $\approx$ 7K-22K and magnetic fields of 0, 4, and 5 Tesla. In addition to these tests, other experiments were conducted without a temperature gradient for comparison. The measured data points for the target breakdown voltage versus helium mass density were plotted in Fig. 4.3. At least three measurements were performed for each condition. Here the mass density was computed considering the helium pressure inside the target and the average temperature of the target during the test.



Figure 4.3: Raw data points of the target breakdown voltage as a function of helium mass density for different B-fields. The latter was computed considering the helium pressure inside the target and the average temperature of the target during the test. The red data points on the right correspond to a target without temperature gradient.
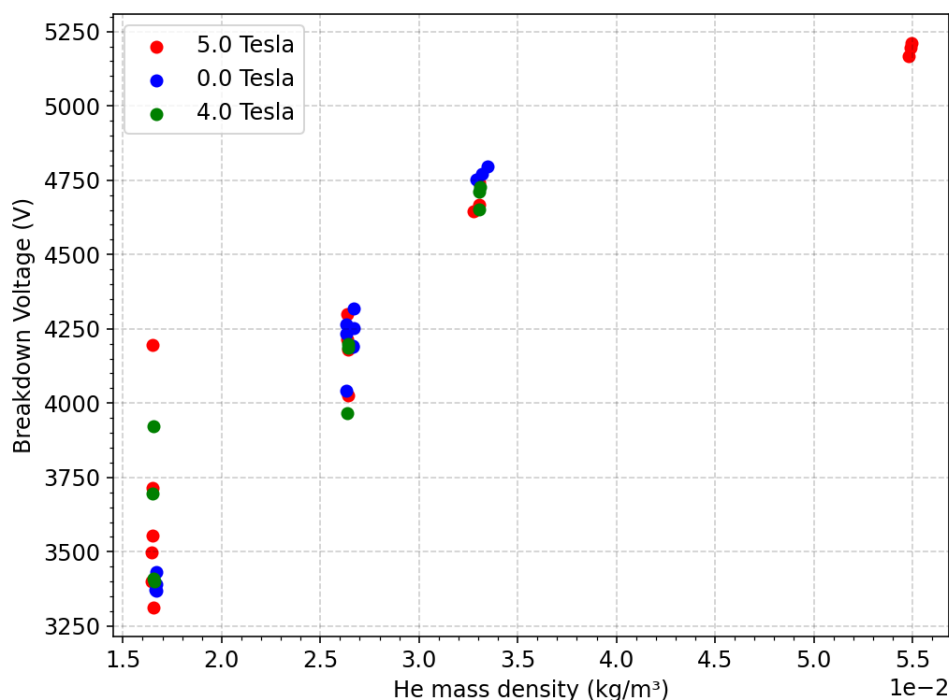
Moreover, the average of the breakdown voltage data for each pressure and magnetic field conditions was computed and plotted in Fig. 4.6. The uncertainty on the voltage was determined

using the standard deviation of the collected data. This is reasonable given the statistical nature of electrical discharge.

Breakdown voltage tests showed distinctive trends influenced by helium pressure, magnetic field, and temperature gradient. Higher helium pressures were consistently associated with higher breakdown voltages. Spark voltages at 10 mbar varied between 4600 and 4800 V. At 8 mbar, the spark voltages were frequently between 4000 and 4300 V. At 5 mbar, the breakdown voltages were the lowest, ranging from 3300 V to 4200 V. The trend of the data is compatible with the Paschen curve of helium for high density levels [11].

A temperature gradient across the target affects the breakdown voltage. The breakdown voltage was reduced when the bottom of the target was cooled to around 7 K and the top was heated to roughly 22 K, compared to when there was no strong temperature gradient present ($\approx 7 - 10$ K). This effect was observed at a pressure of 10 mbar, with the gradient decreasing the breakdown voltages by several hundred volts.

In the case of the tests without a magnetic field, a jump in the resistance of the target at lower voltages was observed. This was found to be pressure dependent: for instance at 10 mbar, a change in the slope of the current-voltage curve occurred at approximately 3000 V, indicating a sudden jump in the resistance value, as shown in Fig. 4.4. Nevertheless, the power supply was capable to keep ramping to high voltages and then another spark occurred.

It was hypothesized that, in the absence of a magnetic field, a small discharge was triggered at relatively low voltage values. This behaviour is likely related to the different trajectory that free electrons undertake in the target when no magnetic field is applied. In contrast, the strong magnetic field appears to prevent the breakdown avalanche by causing gyromotion of electrons, effectively increasing the path that they must travel through the gas, thus reducing the probability of fast ionisation and stabilising the system [12]. Although the exact mechanism remains unclear, it was decided to proceed with the experiment, because this behavior disappeared once a strong magnetic field was applied, which aligns with our area of interest.

Additional tests examined the behaviour with a different power supply that was planned to be used in the 2024 beamtime. As the HV channels are eventually all interconnected through voltage dividers, they are not independent, meaning the current each channel supplies does not only depend on its own voltage. To achieve this, a quadrant power supply capable of push-pull operation was employed.

The same target as in all the other voltage tests was used. But this time, it featured 1 main HV voltage and 4 HV channels in quadrant operation. A summary of the measured data is shown in Fig. 4.6. The most encouraging results were achieved when the quadrant power supply
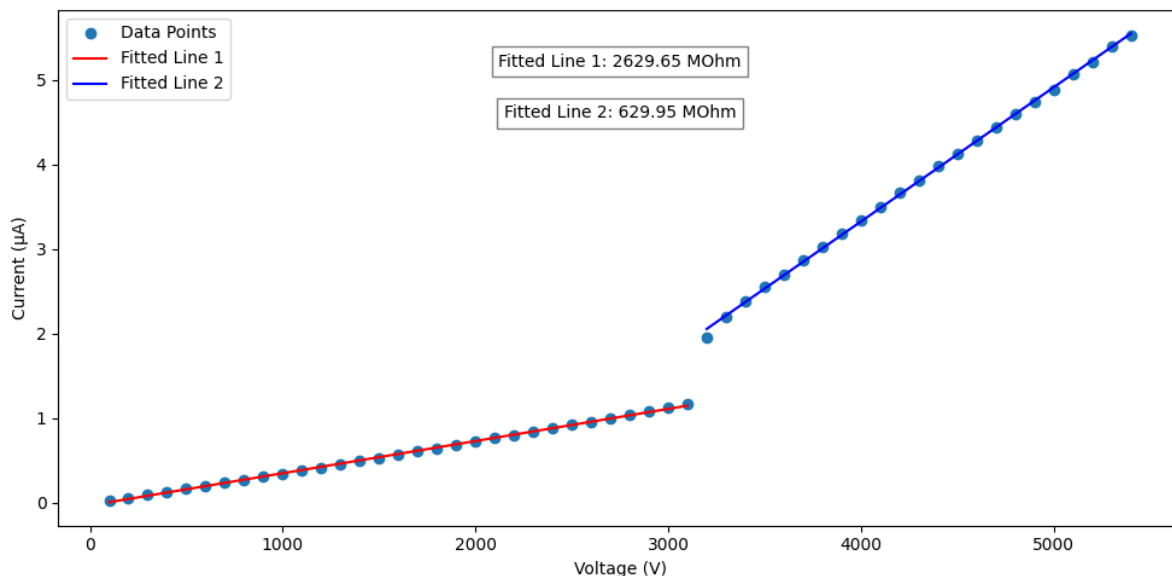
Figure 4.4: Measurement with B = 0 T for a target pressure of 10 mbar and a temperature gradient of 7K / 22K, showing an unexpected current jump at approximately 3000 V, only observed in the absence of a magnetic field.



Figure 4.5: Measurement with B = 5 T for a target pressure of 10 mbar and a temperature gradient of 7K / 22K showing no current jump when the magnetic field is applied.

was combined with high magnetic fields. The green line represents the optimal voltage for stable operation of the muCool target. The breakdown voltage data points lying above this line demonstrate that muCool's working voltage range is achievable.

In summary, higher helium pressures contributed to larger breakdown voltages, strong magnetic

Figure 4.6: Breakdown voltage of the target as a function of the average He gas density for various targets. The green line repr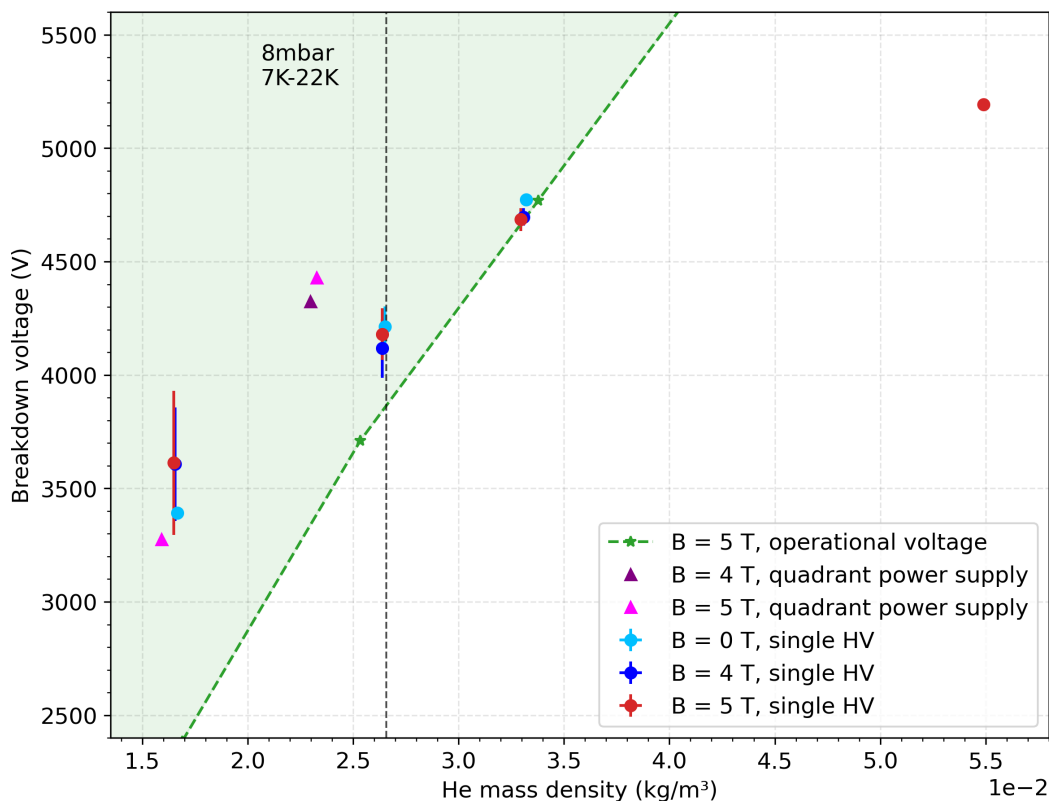esents the optimal voltage required at the given density according to GEANT4 simulations. Targets that are on or above the green line meet our operational requirements. The vertical black line marks a gas density equivalent to 8 mbar and a temperature gradient from 7 K to 22 K.

fields stabilized the system and enabled higher working voltages, while temperature gradients reduced the breakdown voltage values.

Additional measurements were performed to determine the location in the target where the electrical discharge happened. For this purpose an optical window was installed to look inside the vacuum chamber where the target was cooled down and to monitor the spark's position. Observations have been obtained only from one perspective, making it difficult to pinpoint the spark's position along the z-axis. To improve visibility, a mirror was mounted over the target to observe the top wall of the target and determine the spark's z-axis position. These experiments were then recorded using a camera mounted outside the cryostat and focused on the mirror to see not only where the spark happened, but also how the target moves and contracts during cooling.

The first observations suggested that the spark was localised close to the thin Kapton tubes used for filling the target with helium gas. In fact, the presence of materials with sharp edges might

induce discharges because the E-field is enhanced for pointy objects.

However, additional problems arose from the pictures shown in Fig 4.7. At cryogenic temperatures, the kapton foil started to wrinkle between the plastic bar and the sapphire plates due to the different thermal contraction of the materials. And this target's behaviour at low temperatures seemed to be connected to the breakdown voltage, as the discharge arc was observed around this area shown in Fig 4.8. Along with discharge issues, the wrinkling of the Kapton between the sapphire and the plastic bar presented an important challenge, as it affected in the alignment of electrodes at the target's tip in turn distorting the produced electric field close to the orifice region.



Figure 4.7: Kapton attached on sapphire and a plastic bar is shown under several conditions: the left picture at room temperature (300 K), the middle image at cryogenic temperature (22 K), and the right image during electrical discharge.



Figure 4.8: This image combines the previous pictures to help to identify the possible location of the discharge.

To solve these problems, different options were studied, including the application of glue between

sapphire and plastic bar, minimising the gap between them, and further methods in order to maintain a smooth and stable surface of the Kapton and so to reduce the possibility of discharges near the orifice.

One of the most crucial tests was tracking the system's behaviour during the cooling phase. In this experiment, just the bottom sapphire was attached to the Kapton bottom foil, with no Kapton on the top and no electrical connections. This configuration allowed for a focused evaluation of the system's behavior during cooling. The results indicated that the different contraction rates of sapphire and plastic exposed the Kapton to significant stress ultimately causing it to tear. For this porpuse a new glueing technique was developed. By applying glue on the sapphire plate in a triangular shape, the region where the muons are compressed is not affected by the wrinkling, as shown in Fig. 4.9 (top). It succeeded in minimising stress near the orifice. Despite its effectiveness, this method was not consistently reproducible.

This finding marked a turning point, triggering a full redesign of the setup. Cooling would no longer be done with sapphire plates, but with cold helium gas flowing inside plastic plates, and the entire target would be made of plastic. The test described above was repeated glueing the bottom Kapton foil to a plastic plate. Fig. 4.9 (bottom) displays the behaviour at cryogenic temperatures: no wrinkling or tearing of the kapton foil was observed.

In the end, these challenges resulted in the development of a completely plastic target. The Kapton-sapphire assembly's natural tension problems were solved by this new structure, which also significantly improved the setup's robustness. Additionally, internal plastic pins that in the past caused discharges because of their sharp edges could be removed thanks to the entirely plastic target.

The evolution from the sapphire-Kapton structure to a fully plastic design represents a major advancement, addressing both mechanical and electrical issues to create a more reliable and efficient experimental setup.

## 4.3   ESD Coatings

In the muCool target, free charges, like helium ions and electrons (see Chapter 1), are present and can accumulate on the plastic walls of the 3D-printed target frame. An accumulation of charges may distort the applied electric field, thereby affecting muon extraction.

The goal of the study was to develop a solution to solve this problem by creating a substance with specific conductivity to dissipate the accumulated charges. An electrostatic dissipative (ESD) coating, known as an ESD-safe coating for plastic, was applied to the target for this
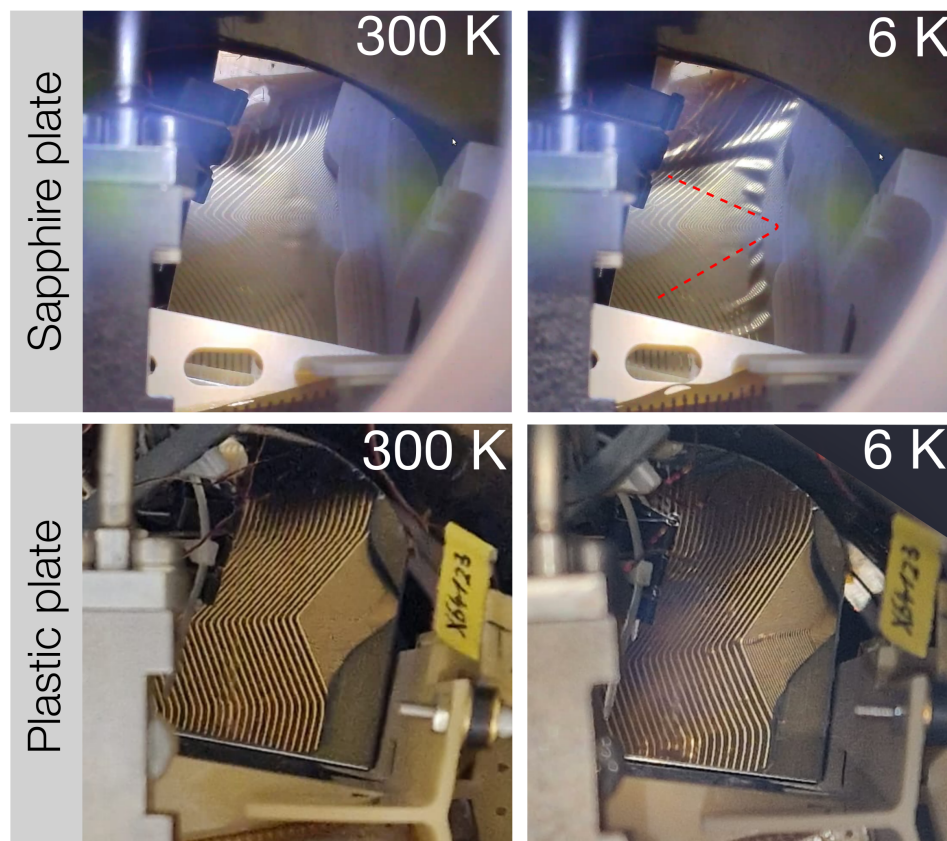
Figure 4.9: (Top row) Image of the bottom target wall glued to the sapphire, illustrating the wrinkling of the Kapton foil at cryogenic temperatures. This is due to the thermal stress between the plastic frame and the sapphire. By applying glue in a triangular shape, the region where the muons are compressed, indicated in red, is not affected by the wrinkling. (Bottom row) Image of the bottom target wall where the sapphire is substituted by a plastic plate glued to the entirety of the kapton foil. Because the bottom wall plate and the target frame are made of the same material, the kapton does not tear or wrinkle at cryogenic temperatures.

purpose. This coating was developed to handle charge buildup effectively, ensuring stable electric field conditions and reliable muon extraction.

The available ESD 844AR liquid products [13] show a surface resistance range of ($10^6 \Omega/sq - 10^8 \Omega/sq$), requiring extensive testing to get an acceptable result. In order to avoid short circuits, the ESD coating areas must have resistance 10–100 times greater than that of the resistors in the target, which are in the range of ($10 \, \text{to} \, 100 \, \text{M}\Omega$).

As the current ESD coatings did not satisfy the resistance criteria, a custom-made solution was created. Stycast epoxy resin [14], a cryogenic glue utilised for target assembly, was combined with conductive powders such as aluminium pyro MT and graphite, both of which were readily

available. Furthermore, commercial ESD liquids and sprays have been mixed with the glue to test their performance.

Considering that Stycast glue is by nature non-conductive, multiple experiments were required to identify the ideal mixture. Exact quantities of conductive material were systematically mixed into the glue. Despite careful efforts, one major challenge was the lack of reproducibility in the measurement results.

Initial tests were performed on Kapton foils containing printed electrodes to optimize the contact of the mixed material with the multimeter. After determining the optimal mixture and method, testing proceeded to Visijet plastic, the material used for the target frame. Specially created bars and frames were used to ensure reliable electrical contact with the in-house made ESD mixture during plastic testing.

The production process of the ESD mixture follows to a standardised approach summarised here:

- Get a beaker with ESD material and measure its weight to 5g.

- Include certain percentages of Stycast glue in accordance with the required formulation.

- Stir the liquid for 30 seconds to 1 minute to guarantee complete integration of the ESD and glue. Effective amalgamation is essential to get the requisite characteristics. An important consideration is the volatility of the ESD material. After the set mixing duration, the mixture must be administered quickly, since its intended effects could be lost if more than 5 minutes pass. Due to its volatile characteristics, it is strongly advised to make and mix the ESD paint inside a fume hood to prevent inhalation of vapours.

- After mixing, the ESD-safe paint must be applied to the selected surface.

- The coated surface is afterwards left to dry at room temperature for 24 hours. For a faster curing procedure, the coating may be positioned in a heated environment, such as a curing box, at 45°C for around 1 hour.

- Upon curing, the resistance over a specified region of the thin layer is assessed using a multimeter that can measure resistances up to the T$\Omega$ resistance ranges to verify that the coating satisfies the required electrical demands.

## 4.4   ESD Coating Results

As mentioned earlier, many experiments were conducted to find the perfect mix for the ESD coating. After many unsuccessful tests with aluminium pyro MT, graphite, and ESD spray,

which failed to generate reliable conductivity observations, we opted to mix ESD liquid with the stycast glue. The idea was to tune the resistivity of the mixture with the relative amount of the substances. The initial tests failed, revealing that the required amount of ESD liquid to be mixed with the Stycast glue needed to be significantly higher than initially expected. Results with a small percentage of stycast are summarised in the table 4.1. These results correspond to three layers of ESD applied to a surface of $1.5\,\text{cm} \times 0.5\,\text{cm}$.

| Test # | Stycast percentage | Measured resistance |
|:---:|:---:|:---:|
| 1. | 1.7% | $\sim 48 - 66\,\text{G}\Omega$ |
| 2. | 2.7% | $\sim 1.6 - 4\,\text{G}\Omega$ |
| 3. | 3.8% | $\sim 26 - 43\,\text{G}\Omega$ |
| 4. | 4.9% | $\sim 31 - 36\,\text{G}\Omega$ |
| 5. | 6.1% | $\gtrsim 100\,\text{G}\Omega$ |
| 6. | 7.1% | $\gtrsim 100\,\text{G}\Omega$ |

Table 4.1: Test results for ESD with different percentages of Stycast glue, showing corresponding resistance ranges.

The results showed that ESD liquid combined with a $\sim 2\%$ concentration of Stycast glue, as in Test 1, is the best option. Tests 2, 3 and 4 in the table were within the expected resistivity range, but at this concentration, reproducibility remained a problem. Therefore, the 2% concentration was chosen for further testing.

A further test was to evaluate the ESD coating's performance at cryogenic temperatures at which the target operates. For this purpose, a Kapton foil with printed copper lines without resistors, was glued to the frame and the frame was painted with ESD considering to connect the ESD also to the copper lines of 1.5 mm separation from each other. In order to conduct the test, cables were soldered to copper lines that were interconnected via the ESD coating.

The resistance of the ESD mixture was measured at cryogenic temperatures, and their values were within the same range as those measured at room temperature.

As mentioned in the previous section, it is probably essential to apply the ESD coating to the target walls to prevent the distortion of the applied electric field caused by accumulated charges on the walls. The mixture was applied uniformly with a brush to the target frame, as shown in Fig. 4.10, and a major advantage of the ESD was its weakly adhesion to the Kapton foil, allowing accurate painting of the frame and effective attachment of the copper lines on the Kapton.

The application of paint close to the orifice was very critical. The coating needed to cover the plastic and make contact with the Kapton, especially on the copper lines. The small dimensions

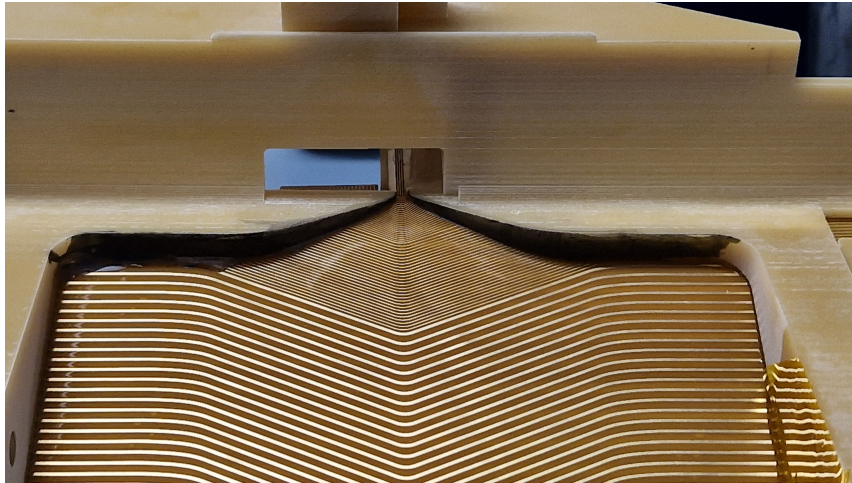of the aperture (1.3 mm x 1 mm) made accurate painting a difficult task. The result is shown in Fig. 4.11.



Figure 4.10: The internal walls of the muCool beamtime target painted with a mixture of electrostatic dissipative (ESD) liquid and $\approx 2\%$ stycast glue.



Figure 4.11: Zoomed-in view of the orifice on the muCool beamtime target with applied ESD + stycast glue mixture.
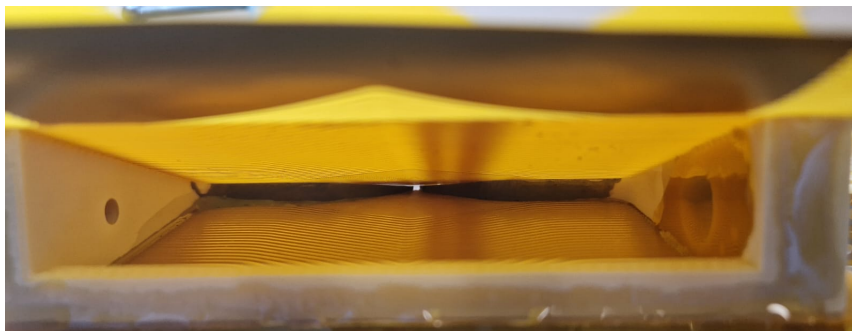


Figure 4.12: muCool 2024 beamtime target with applied electrostatic discharge (ESD) during assembling.

After applying the ESD coating, the target was ready for the next step, which included glueing the top wall of the target to the plastic frame. Fig. 4.12 shows the inside of the beamtime target after this stage.

## 4.5   Conclusion

In this chapter breakdown test of the muCool target were conducted. It was found that the highest applicable voltages were compatible with the simulation requirements. During the experiments, wrinkles of the kapton foil in the front of the target were observed at cryogenic temperatures. This was due to the thermal contraction mismatch between sapphire and plastic. The wrinkle on the kapton was considered to be a major cause of electrical breakdown. The change from a sapphire plastic target to a fully plastic target not only solved the wrinkle problem but also guaranteed that the copper lines printed on the Kapton were aligned at the orifice, allowing the generation of the desired electric field.

Furthermore, the redisegn of the target offered major advantages in both the assembly process and robustness.

The application of Electrostatic Dissipative (ESD) liquid on the target plastic frame to disperse accumulated charges on the target gave promising results. The most promising result was obtained using a mixture of commercially available ESD liquid with 2% amount of Stycast glue. Future study is required to achieve a better understanding of how the ESD material behaves at cryogenic temperatures, which will help in the validation of these results under the full muCool operational conditions.

# Chapter 5

# Detection of positrons

The previous chapters discussed the thermal and electrical stability of the muCool target. Within the target, muons drift under the combined influence of the electric field, magnetic field, and collisions with helium gas.

To study muon motion and validate the target's performance, scintillators are placed outside the target to detect positrons produced by muon decay (See Fig. 5.1). These scintillators form telescopes with limited geometrical acceptance, designed to focus on specific regions of interest. Observing particle compression and extraction requires the detectors to be precisely positioned and read out in pairs to ensure optimal coverage and accuracy.

To further improve the spatial resolution of these detector pairs, they are mounted inside a copper collimator. The collimator suppresses positrons originating from muon decays occurring far from the scintillators, reducing background noise and improving the signal-to-noise ratio. However, the 3D-printed plastic design of the extraction region in the target introduces mechanical constraints that prevent the use of copper collimation in this area.

To address these challenges and maintain consistent detector performance, simulations were conducted to optimize the position and alignment of the detectors. These simulations, performed using the Geant4 toolkit [15], modeled the interactions of muons and positrons with the target geometry and surrounding materials. The optimization focused on maximizing detection efficiency and spatial resolution while minimizing background contributions.

As a result, the performance of the detectors in the extraction region relies solely on the careful optimization of the scintillators' position and geometry, informed by detailed Geant4 simulations. These efforts ensure the reliability and precision of the detector system, even in the absence of copper collimation.
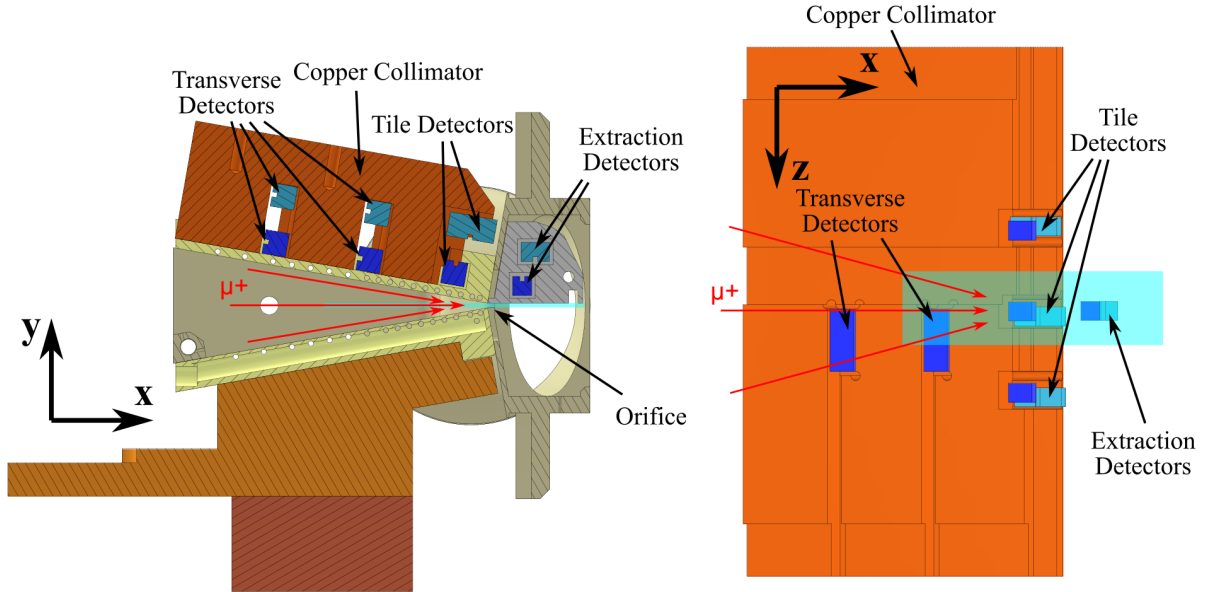
Figure 5.1: Detector placement: The teal region indicates the area where muons are generated.
(Left) Side view cross-section of the target at $z = 0$, showing detector positions relative to the plastic frame.
(Right) Bottom view of the collimator with the detector arrangement

## 5.1 Detector Simulations Using Geant4

Geant4 is a versatile Monte Carlo simulation toolkit [15] designed for modeling particle interactions with matter using probabilistic methods. It allows for detailed simulations of processes such as scattering, energy deposition, and particle decay. The toolkit is capable of tracking particle trajectories through complex geometries, accurately modeling their interactions with materials and the surrounding environment. Additionally, Geant4 enables the definition of intricate experimental setups, including their geometry and material composition, providing a highly customizable framework for simulation.

This work focuses on optimizing the detectors and their placement in the extraction region, where space is highly constrained. The optimization process was constrained by practical factors, such as preserving the target's leak-tightness and integrating the detector holders without compromising stability. These requirements ensured that the final design remained both functional and fully compatible with the experimental setup.

The maximum size of a scintillator was set at $6 \times 4 \times 4 \text{ mm}^3$, with the detectors confined to a space no greater than $\pm 14$ mm in the vertical direction. Each simulation involved 100,000 muon decays, enabling a direct comparison of results. The muon decays were generated uniformly

within a defined volume along the x-axis ($\Delta x \times \Delta y \times \Delta z = 60 \times 1.5 \times 10 \text{ mm}^3$) (the teal-coloured zone on Fig. 5.1). While the scintillator thickness in the z-direction was fixed at 4 mm, the x- and y-dimensions were varied across different configurations.

To achieve efficient detection of muons within the region of interest while suppressing the detection of positrons from decays occurring outside this region, the simulation included two pairs of scintillators positioned above and below the extraction region in a mirrored arrangement (See Fig. 5.2). Each pair consisted of two scintillators stacked vertically with a small gap between them. The scintillators in these pairs had fixed dimensions of $4 \times 4 \times 4 \text{ mm}^3$, ensuring consistent performance during the optimization process.
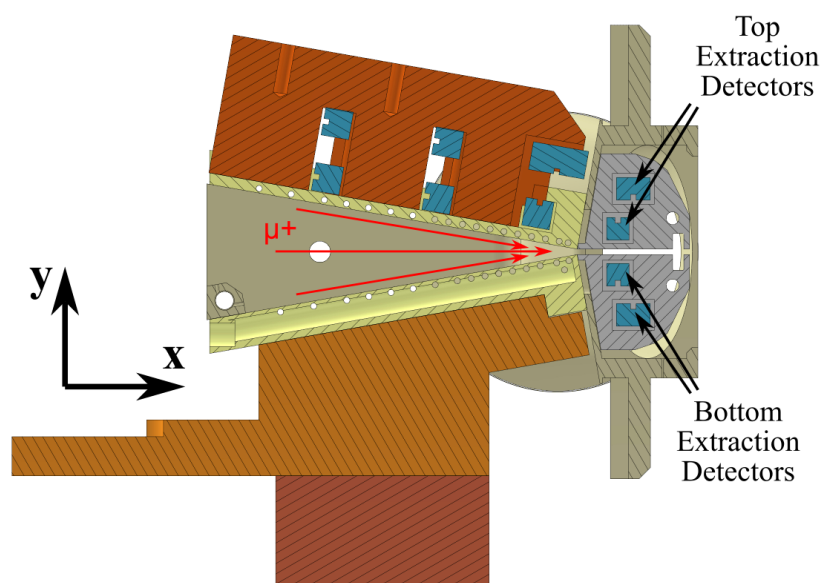


Figure 5.2: Detectors placement including 4 extraction detectors.

The simulation results are presented in Fig. 5.3. The left column displays the xy-projection of detected positrons for each pair of scintillators, while the middle column shows the corresponding xz-projections. The top row represents the results for scintillators positioned above the extraction line, whereas the bottom row corresponds to those located below it. The right column contains 1D spatial histograms, illustrating the number of detected positrons (counts) as a function of position along the x-axis. For all these plots we have assumed 0.2 MeV energy deposition in each scintillator and we have required a coincidence detection.

The 1D spatial histogram reveals that the scintillators below the extraction line detect a significant amount of muons still within the target, leading to the appearance of a tail in the spectrum. Since this tail originates from muons in the target or near the orifice entrance, it does not
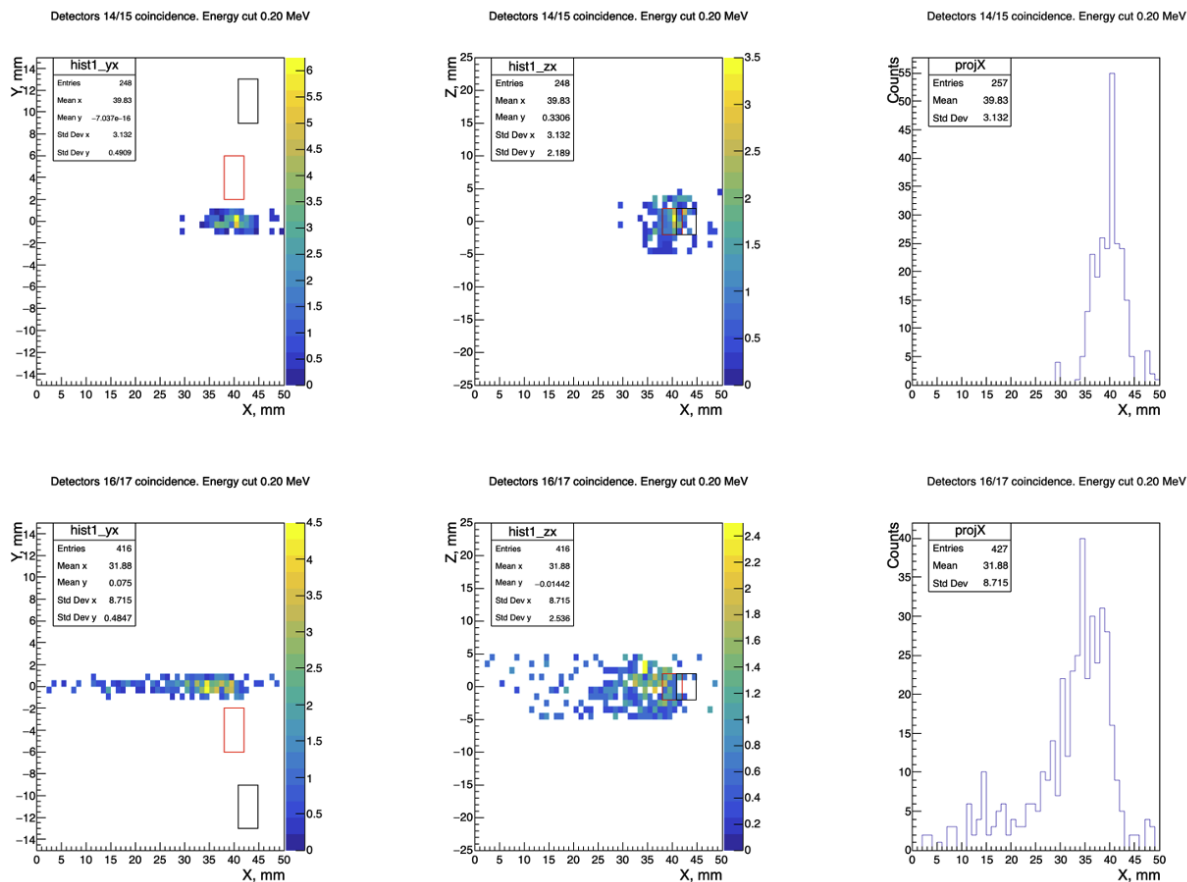
Figure 5.3: Simulation results for the positions of $4 \times 4 \times 4$ mm$^3$ scintillators in relation to the extraction lines: The upper graph shows scintillators positioned above the lines, while the lower graph illustrates those situated below. Red and black boxes represent scintillators.

provide a clean information only on the extracted muons. The difference originates from the B-field wich is breaking the symmetry of the problem. Consequently, the analysis was focused on the scintillators above the extraction line, and the bottom pair was removed to simplify the detection system. The top pair of scintillators alone provides sufficient information to confirm muon extraction while reducing system complexity.

Another part of the simulation aimed to determine the optimal detector size within the limited available space, balancing detection efficiency (statistical performance) and spatial resolution. Two sets of model configurations were explored to evaluate different scintillator arrangements.

In the first configuration (Fig. 5.4), both scintillators in the pair were identical, with dimensions of $4 \times 4 \times 4$ mm$^3$, $3 \times 3 \times 4$ mm$^3$, and $2 \times 2 \times 4$ mm$^3$. The bottom scintillator remained fixed in position, while the top scintillator was shifted upward by 1 mm.

In the second configuration (Fig. 5.5), the top scintillator was fixed at $6 \times 4 \times 4$ mm$^3$, while the bottom scintillator was tested in two different sizes: $6 \times 4 \times 4$ mm$^3$ and $4 \times 4 \times 4$ mm$^3$. In this case, the centers of both scintillators remained fixed.
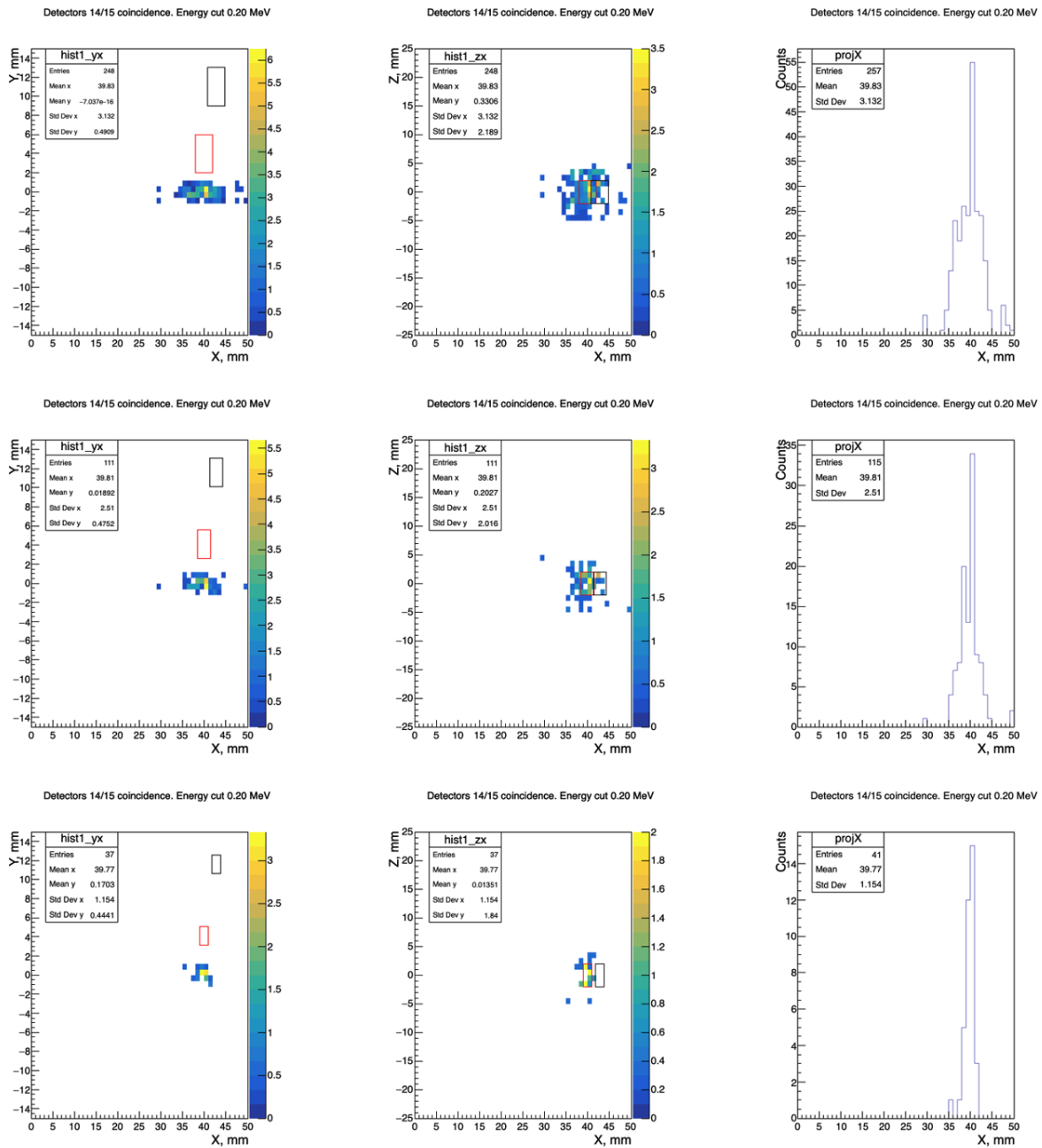


Figure 5.4: Simulations results for different scintillator sizes.
Top: Scintillator with dimensions $4 \times 4 \times 4$ mm$^3$.
Middle: Scintillator with dimensions $3 \times 3 \times 4$ mm$^3$.
Bottom: Scintillator with dimensions $2 \times 2 \times 4$ mm$^3$.

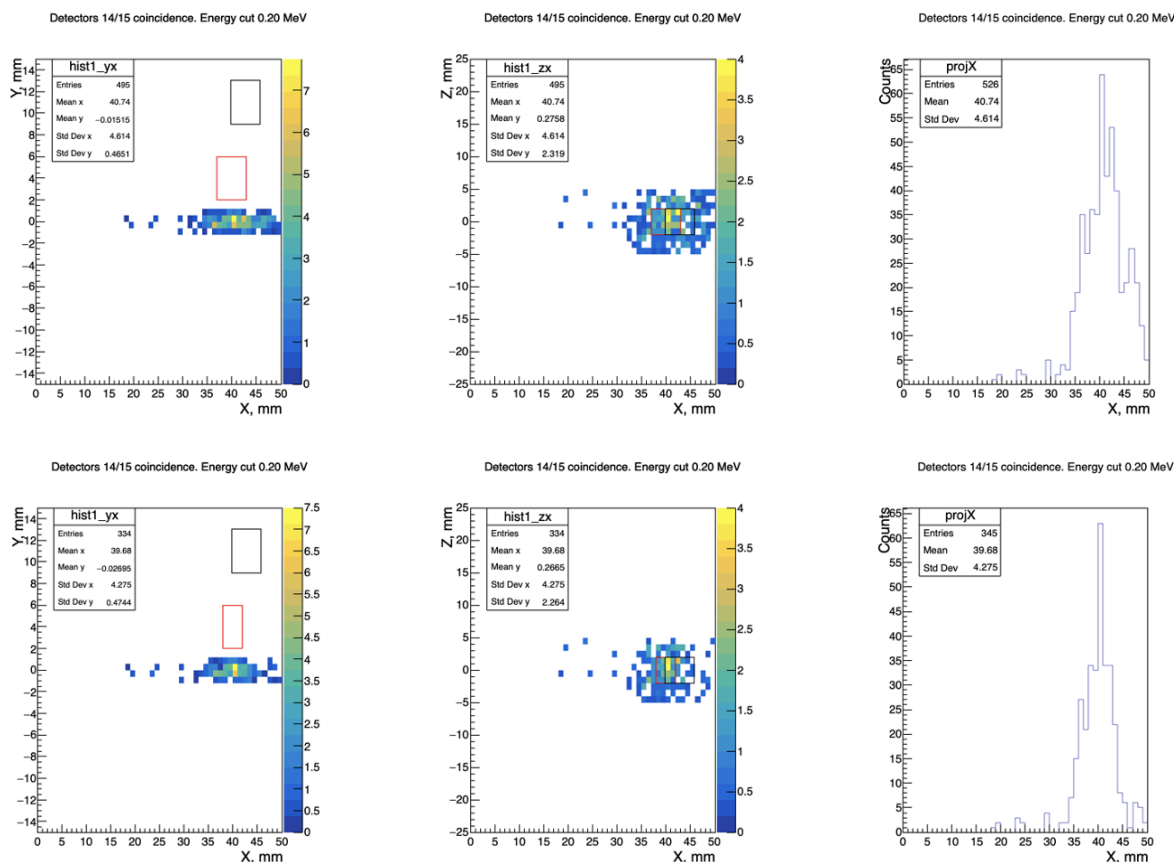The results demonstrate a significant impact of scintillator size on detection efficiency. Larger

Figure 5.5: Simulations results for different scintillator sizes.
Top: Scintillator with dimensions $6 \times 4 \times 4\text{mm}^3$.
Bottom: Scintillator with dimensions $4 \times 4 \times 4\text{mm}^3$ and $6 \times 4 \times 4\text{mm}^3$.

detectors ($4 \times 4 \times 4\text{mm}^3$) outperformed smaller $3 \times 3 \times 4\text{mm}^3$ detectors, as their increased coverage above the extraction lines led to higher positron detection rates. In contrast, the smallest detectors ($2 \times 2 \times 4\text{mm}^3$) detected fewer events than their larger counterparts, with the detection count not scaling proportionally to their volume. This discrepancy arises from the coincidence condition applied in the simulations, which causes a nonlinear decrease in detection efficiency as detector size decreases.

The simulations confirmed that increasing detector size enhances positron detection, providing better statistical accuracy. However, this improvement comes at the cost of spatial resolution.

As shown in Fig. 5.5, the configuration using the largest detectors ($6 \times 4 \times 4$ mm$^3$) resulted in a count rate 1.5 times higher than the setup combining a smaller detector ($4 \times 4 \times 4$ mm$^3$) with a larger one ($6 \times 4 \times 4$ mm$^3$). Despite the higher count rate, the latter configuration provided a significant improvement in spatial resolution.

Based on these findings, the most effective detection setup consists of a smaller detector positioned near the extraction region and a larger one placed above it. This configuration balances detection resolution and statistical performance while accounting for the physical constraints of the setup.

## 5.2 Implementation

With the detector design established through simulations, the next step is its practical implementation. The finalized detector system (Fig. 5.1) consists of six telescopes, each comprising a pair of scintillator counters stacked with a small gap between them. The gap maximum was dictated by the maximal bending radius in the B-field. These pairs operate in coincidence to enhance spatial resolution. One telescope is positioned above the extraction region, serving to determine whether muons are successfully extracted from the target. The remaining telescopes are placed just above the target volume to monitor muon behavior within the target, specifically providing insight into muon compression.

With the exception of the two scintillators near the extraction region, all scintillators were enclosed within a copper collimator to further improve spatial resolution by suppressing unwanted positrons from decays occurring outside the region of interest.

A basic scintillator counter consists of a scintillator coupled to a SiPM. However, the SiPMs used in this experiment exhibit reduced efficiency in the 20–40 K temperature range (see Fig. 5.6), which corresponds to the temperature above the target (see Fig. 3.1), where the scintillators—and consequently the SiPMs—must be mounted. To overcome this limitation while also addressing space constraints, a wavelength-shifting fiber (see Fig. 5.7) was used to guide photons from the scintillator to a SiPM positioned in a region with a significantly higher temperature (about 100 K), ensuring optimal detector performance.
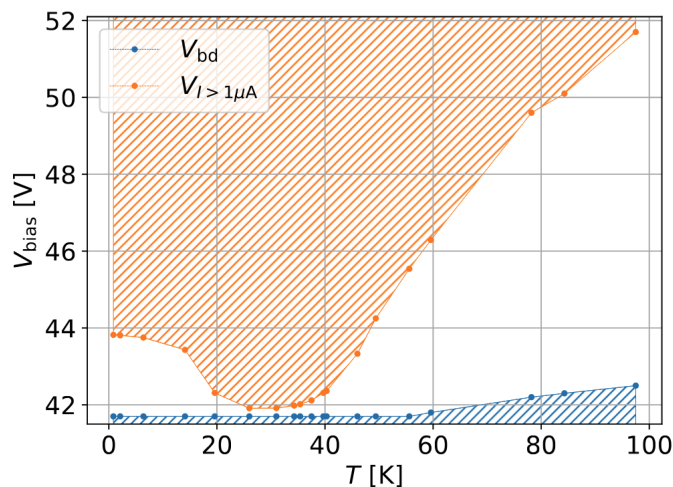
Figure 5.6: Effective SiPM working range for detecting a single photon. The unshaded region is where the SiPM work in Geiger-mode in the cold. At temperatures between 20 K and 40 K, SiPM are unreliable [16].
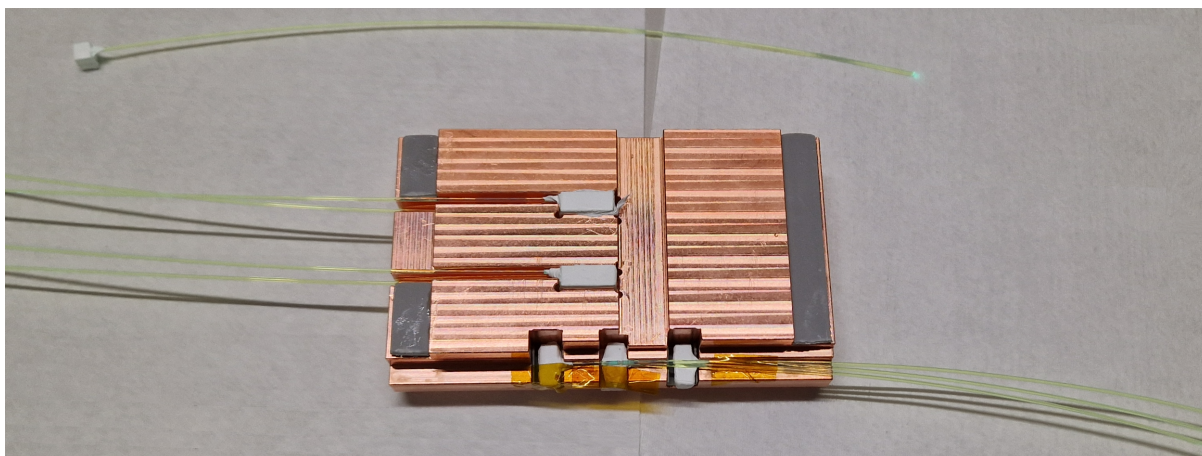


Figure 5.7: Photo of the collimator with transverse, tile detectors, and wavelength-shifting fibers installed.

Wavelength-shifting fibers with two different diameters (0.8 mm and 1.0 mm) were tested at room temperature to determine the optimal coupling method with the SiPM and to select the fiber diameter that provides the best signal-to-noise ratio. To replicate real experimental conditions, a $\beta$ source (Strontium-90) was used, as it emits the same type of particles that the muCool experiment is designed to detect.

To ensure consistent testing conditions, a 3D-printed holder was fabricated to maintain a fixed distance between the $\beta$ source and the scintillator. Additionally, another 3D-printed holder was designed to secure the SiPM, circuit board, and fiber at a constant distance, ensuring repeatability in the measurements. The tests (see Fig. 5.8) demonstrated that a fiber diameter

of 1.0 mm provided the most effective signal detection and was selected for use during beamtime [17].
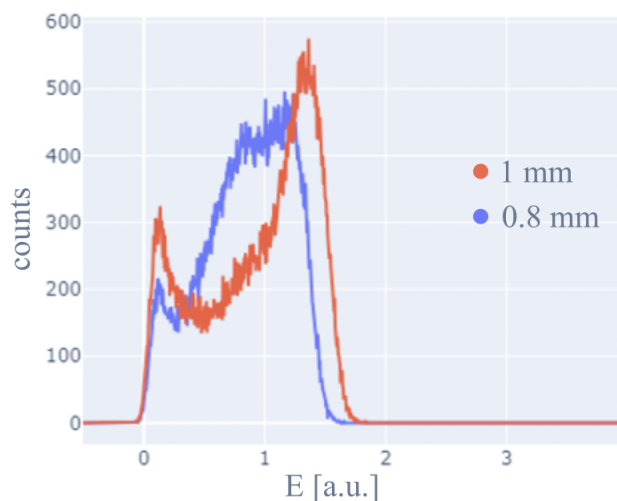


Figure 5.8: Energy spectrum of $4 \times 4 \times 4$ mm$^3$ plastic scintillator read out with 30 cm long wavelength-shifting fibers followed by SiPM (Hamamatsu) for different diameters of the fibers [17].

A key challenge was maintaining stable contact between the fibers and the SiPM under cryogenic conditions, as thermal contraction during cooling could disrupt the connection. Gluing the fibers to the SiPM was not a viable solution, as thermal stress could cause the bond and the detector to break. To address this issue, a specially designed 3D-printed holder was developed to securely position the fibers, ensuring constant and reliable contact with the detector. The fibers were mounted so that their tips remained in contact with the SiPM due to pressure exerted by the natural curvature of the fiber (see Fig. 5.9), maintaining stable optical coupling even under cryogenic conditions (even after the fiber has contracted).
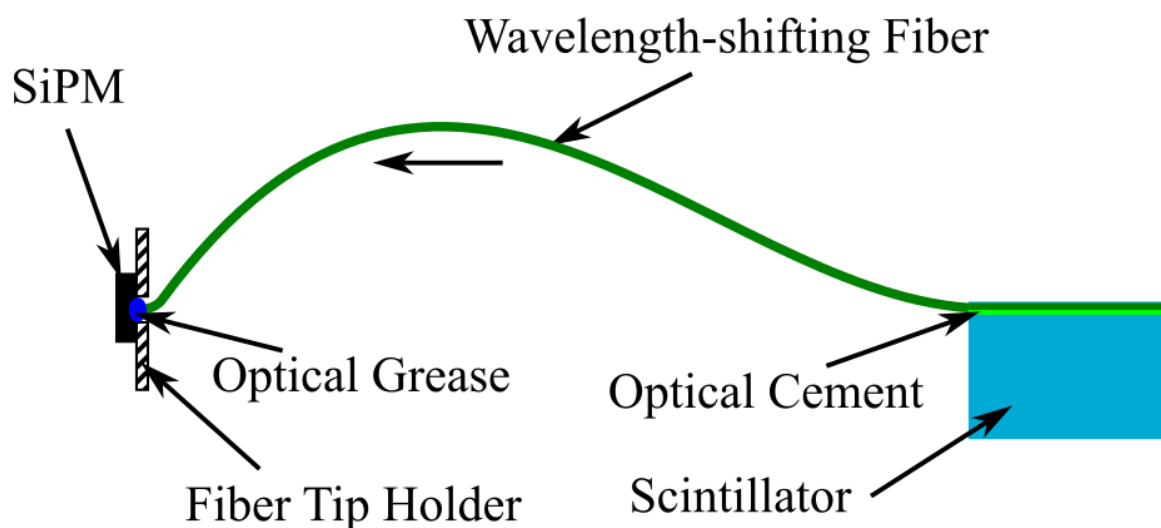
Figure 5.9: Schematic view of the scintillator-WSF-SiPM mounting.

To address these challenges, the tests were essential in understanding the system's behavior under experimental conditions. The scintillators used in the original experiment were tested, each featuring a groove where fibers of different diameters were placed and glued with optical cement. The fibers were then polished at the other end, where the SiPM is placed, to guarantee optimal contact.

Another key aspect of the study was determining whether optical grease was necessary to minimize signal loss and enhance the coupling between the fiber and the SiPM. However, its performance under cryogenic conditions was uncertain. To clarify this, dedicated tests were conducted at the beginning of the beamtime to evaluate the effect of optical grease. The results showed no significant difference in the recorded signal with or without grease. Given the uncertainty of its behavior at low temperatures and the minimal impact on signal quality, it was decided to proceed without optical grease.

Additionally, two SiPM sizes ($1.3 \times 1.3$ mm and $2 \times 2$ mm) were tested. The larger format was selected because thermal contraction could cause the light cone from the fibers to expand beyond the smaller $1.3 \times 1.3$ mm SiPM, leading to signal loss.

Figures 5.10 and 5.11 present an Inventor CAD rendering of the complete detector setup and its photo, emphasizing the scintillator holders previously discussed in the simulation section. A zoomed-in photo is shown in Fig. 5.12. Given the limited space available, the design was carefully optimized to achieve the highest possible spatial resolution.
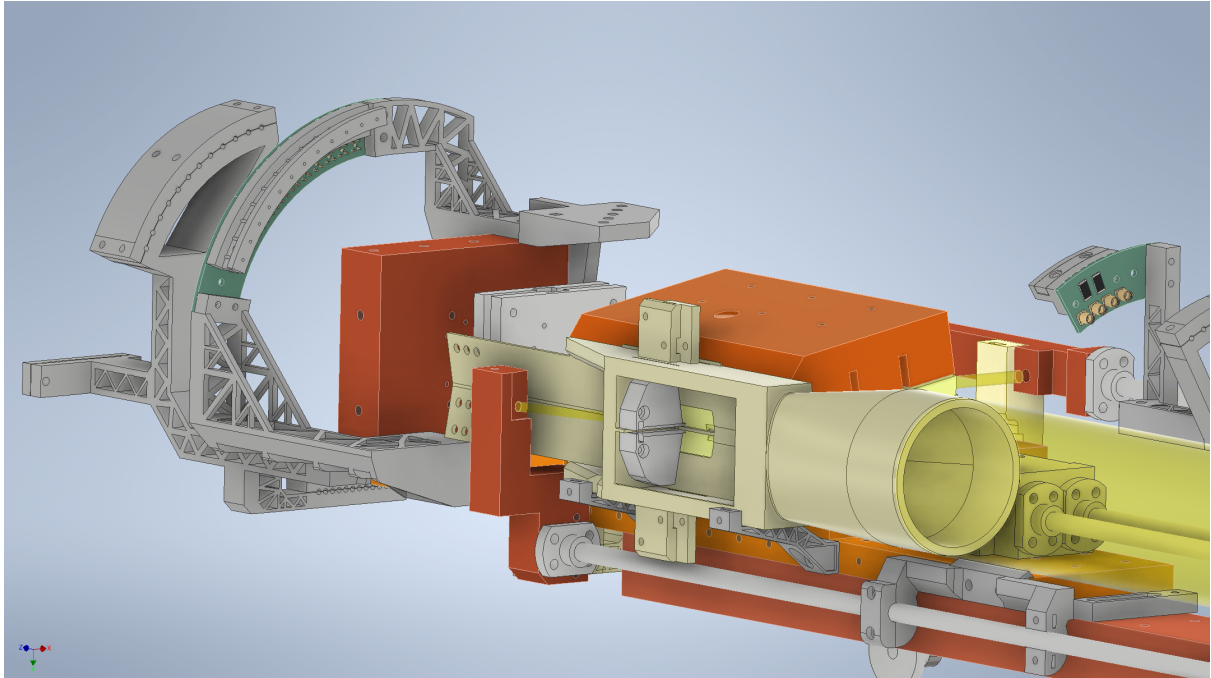
Figure 5.10: Inventor CAD drawing of the complete detector setup without the wave-shifting fibers.
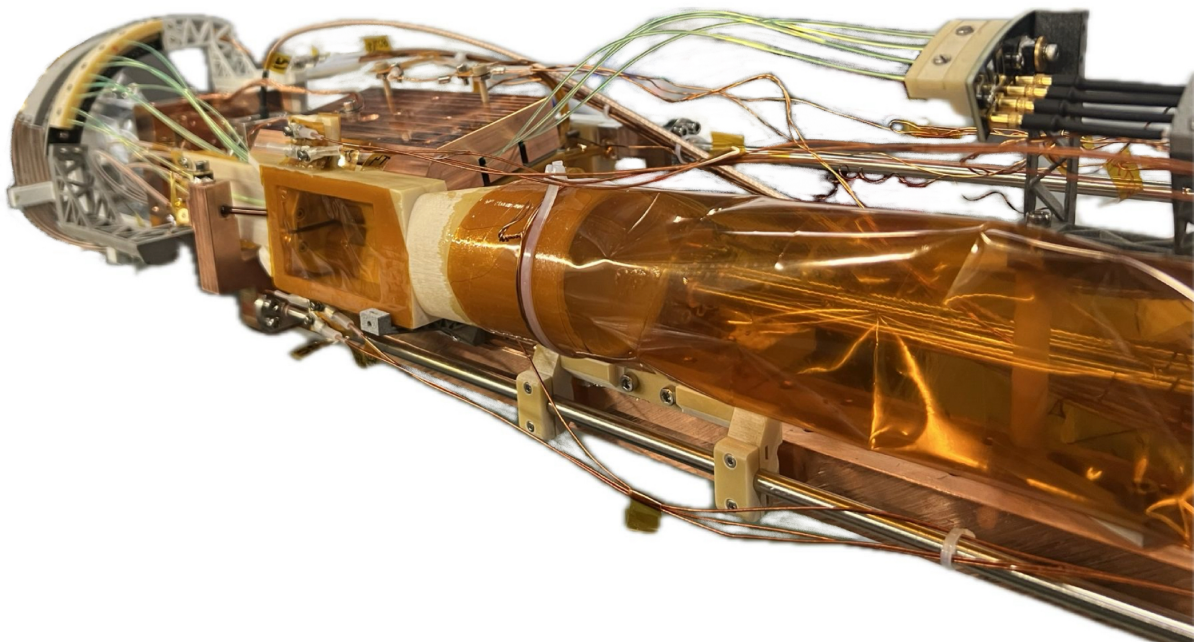


Figure 5.11: Fully assembled target with the installed wavelength-shifting fibers.
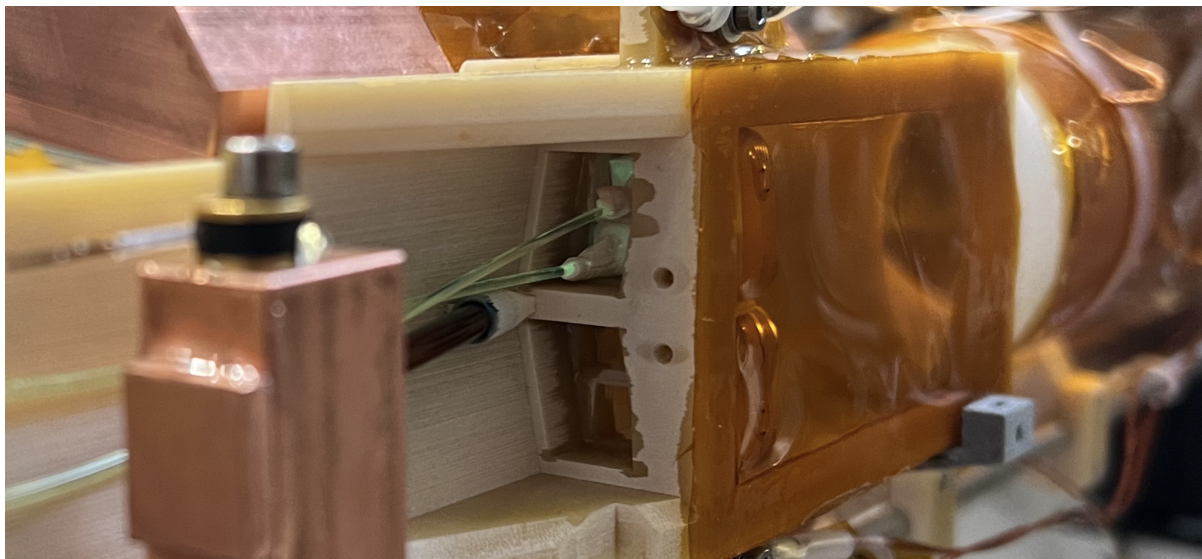
Figure 5.12: Zoomed-in photo of the scintillators in the extraction region with wavelength-shifting fibers.

With these preparations, the setup was ready for the scheduled beamtime in December 2024 at the $\pi E1.2$ beamline of the Paul Scherrer Institute (PSI, Villigen, Switzerland) proton accelerator.

## 5.3 Conclusion

The study focused on optimizing the detection system for muon extraction in the muCool experiment at PSI. Using Geant4 simulations, different detector configurations were analyzed to maximize detection efficiency while maintaining spatial resolution within the constraints of the experimental setup. The results showed that a combination of smaller and larger scintillators positioned above the extraction region provided the best balance between resolution and statistics, ultimately leading to the decision to eliminate the bottom detector pair to simplify the system.

Further optimization efforts examined the impact of scintillator size on detection efficiency, with larger scintillators demonstrating higher positron detection rates but at the cost of spatial resolution. The final design adopted a configuration where a smaller scintillator was placed near the extraction region and a larger one positioned above, ensuring optimal signal detection while minimizing complexity.

To address challenges posed by cryogenic conditions, wavelength-shifting fibers were tested for coupling scintillators to SiPMs, allowing the SiPMs to operate in a higher-temperature region (about 100 K). Extensive testing at room temperature determined that a 1.0 mm fiber diameter provided the best signal-to-noise ratio. A custom 3D-printed fiber holder was developed

to maintain stable optical contact between the fiber and SiPM under thermal contraction, eliminating the need for optical grease.

The final detector system was designed to optimize signal detection while accounting for thermal and spatial constraints. Additional simulations and preparatory studies were conducted to ensure the setup was robust and capable of accurately detecting extracted muons. Additional analysis and validation will help further refine the system and provide a more detailed characterization of its performance under experimental conditions.

# Chapter 6

# Conclusion

This thesis presented a thorough examination of crucial aspects of the muCool experiment, which aims at developing a novel method for producing high-quality, low-energy muon beams. It includs the design, modelling, and experimental validation of essential components of the muCool target system.

Key contributions included heat transfer simulations and experimental tests to investigate how to mantain a vertical temperature gradient throughout the muCool target. The investigation led to the concept of an entirely plastic, helium-cooled target design that effectively solved significant challenges in temperature control and electrical stability. This redesign increased cooling efficiency while also addressing concerns such as breakdown voltages and surface imperfections.

The use of Electrostatic Dissipative (ESD) liquid was also examined to prevent stay electric fields produced by free charge accumulation on the target wall. The development of a technique to guarantee enough electrical conductivity on the plastic frame to disperse free charges offered promising results, but additional testing is required to confirm the behaviour of ESD material at cryogenic temperatures.

The muon detection system around the extraction region was optimised through Geant4 simulations by varying scintillator size and position. The study resulted in a configuration of plastic scintillators around the target and the extraction region that effectively balances detection efficiency and spatial resolution. Wavelength-shifting fibers and a special fiber holder ensured stable contact between the fiber and the SiPM, enabling accurate signal detection in the cryogenic environment.

These studies were performed in preparation of the muCool 2024 beamtime aimed to test for the first time a target designed for phase space compression and muon extraction. This marked an

important step towards the generation of a new muon beam of low energy and small phase space, desirable for future precision particle physics experiments and material science applications.

# Chapter 7

# Appendix

## 7.1 Temperature Sensors

The muCool experiment requires precise temperature control. For this reason, well-calibrated temperature sensors are crucial, particularly in the presence of high magnetic fields. Cernox temperature sensors are excellent for strong magnetic fields ($> 3$ Tesla), whereas Silicon Diodes are typically used in low magnetic fields.

muCool needs to control the temperature at multiple positions. For this purpose, 10 sensors are needed for beamtime.

Cernox sensors will be mounted directly on the target and near the SiPM in locations with a magnetic field of 5 T, and the sensors will be operational at temperatures ranging from a few millikelvin to 100 K. The additional silicon diode sensors will be put in areas with low magnetic fields.

As part of this preparation, a total of 21 temperature sensors were assembled or repaired and then calibrated to ensure accuracy in the data.

### 7.1.1 Silicon Diodes

Silicon diodes transmit current in a single direction, with zero resistance in the forward direction and a high (preferably infinite) resistance in the reverse. This behavior is caused by the sensor's use of semiconductor materials. Typically, a silicon diode has a forward voltage drop, known as a p-n junction, which decreases linearly with temperature. The voltage drop is directly connected to the temperature, due to the temperature dependence of the semiconductor's bandgap energy:

$$V_f = A - B(T). \tag{7.1}$$

- $V_f$ represents the forward voltage drop.

- $A$ is a constant that depends on the material and applied forward current.

- $B$ is a temperature-dependent coefficient.

- $T$ represents temperature in Kelvin.

Each silicon diode responds in this form, and the Lakeshore display device uses pre-saved curves to monitor its output.
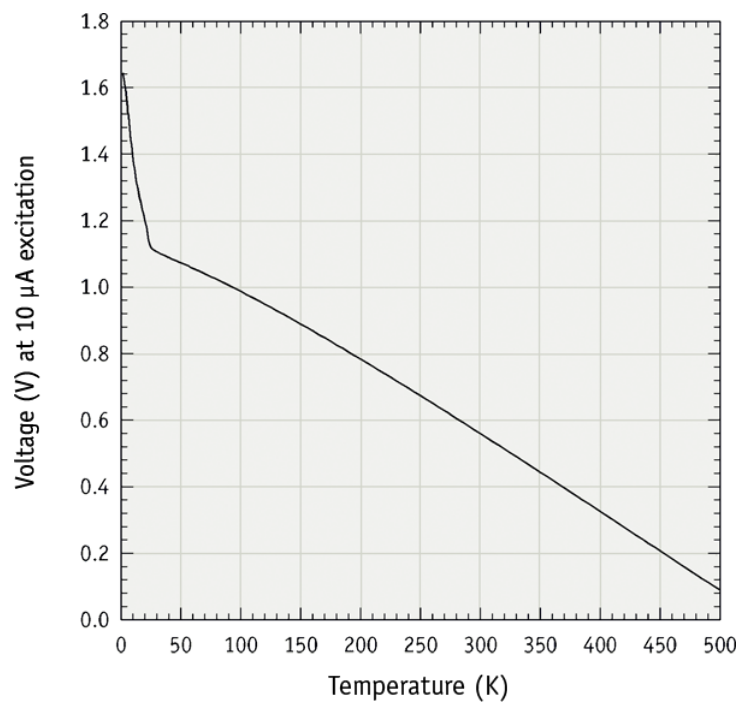


Figure 7.1: This is a usual silicon diode curve which is used to determine the temperature depending on the voltage of the diode. [18]

However, the value of A varies somewhat between various types of diodes, requiring separate calibration to ensure accurate temperature measurements.

### 7.1.2 Cernox

Cernox sensors are attractive given their sensitivity and stability across a large temperature range, from millikelvin to several hundred Kelvin. These thin-film resistors built of zirconium oxynitride have a low sensitivity to magnetic fields, making them excellent for muCool studies. Cernox sensors operate on the basis of the material's resistance, which varies with temperature. Cernox sensors, unlike diodes, do not follow a preset curve, hence they must be calibrated by measuring their resistance at various temperatures:

$$R(T) = R_0(1 + \alpha(T)). \tag{7.2}$$

- $R_0$ stands for resistance at a reference temperature (often room temperature).

- $\alpha(T)$ is a temperature-dependent coefficient determined by the behavior of the material.

During calibration, the resistance and temperature of each Cernox sensor is recorded. In Fig 7.2 the curve of a calibrated Cernox sensor is shown.
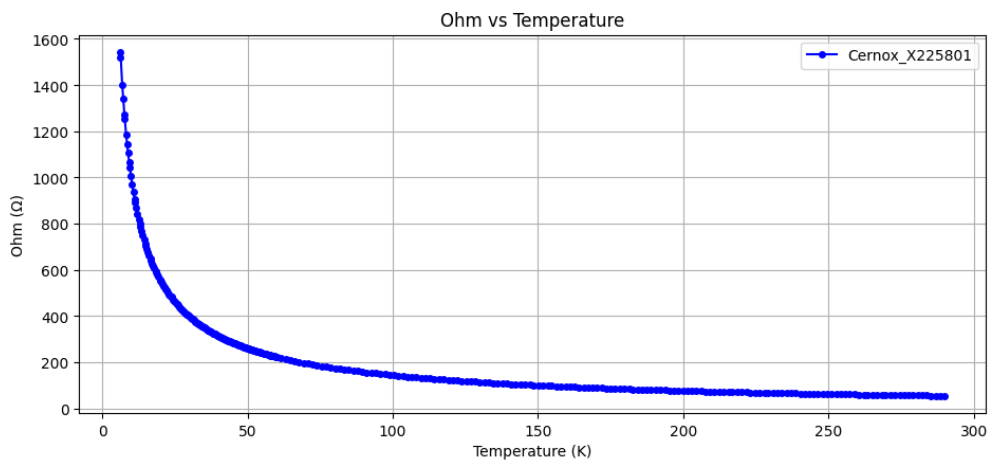


Figure 7.2: This is a standard Cernox curve, illustrating the characteristics of the Cernox sensor with serial number X225801, calibrated by the muCool collaboration.

Once calibrated, these sensors are ready to be installed on the target.

# Bibliography

[1] T. P. Gorringe and D. W. Hertzog. Precision muon physics, 2015. URL https://arxiv.org/abs/1506.01465.

[2] A. Yaouanc and P. de Reotier. *Muon Spin Rotation, Relaxation, and Resonance: Applications to Condensed Matter.* International Series of Monographs on Physics, OUP Oxford, ISBN 9780199596478, 2011. URL https://global.oup.com/academic/product/muon-spin-rotation-relaxation-and-resonance-9780199596478.

[3] Giuseppe Lospalluto, A. Antognini, I. Belosevic, V. Bondar, M. Hildebrandt, R. Iwai, K. Kirch, A. Knecht, P. Mullan, J. Nuber, A. Papa, J. Peszka, M. Sakurai, Ivan Solovyev, D. Taqqu, B. Vitali, and T. Yan. Towards muon cooling at the Paul Scherrer Institute. *PoS*, Muon4Future2023:009, 2024. doi: 10.22323/1.452.0009. URL https://pos.sissa.it/452/009/.

[4] Ivana Belosevic. *Simulation and experimental verification of transverse and longitudinal compression of positive muon beams: Towards a novel high-brightness low-energy muon beam-line.* Doctoral thesis, ETH Zurich, Zurich, 2019. URL https://doi.org/10.3929/ethz-b-000402802.

[5] D. Taqqu. Compression and extraction of stopped muons. *Phys. Rev. Lett.*, 97:194801, Nov 2006. doi: 10.1103/PhysRevLett.97.194801. URL https://link.aps.org/doi/10.1103/PhysRevLett.97.194801.

[6] Ivana Belosevic, Aldo Antognini, Yu Bao, Andreas Eggenberger, Malte Hildebrandt, Ryoto Iwai, Daniel M. Kaplan, Kim Siang Khaw, Klaus Kirch, Andreas Knecht, Angela Papa, Claude Petitjean, Thomas J. Phillips, Florian M. Piegsa, Narongrit Ritjoho, Alexey Stoykov, David Taqqu, and Gunther Wichmann. mucool: a novel low-energy muon beam for future precision experiments, April 2019. ISSN 1572-9540. URL http://dx.doi.org/10.1007/s10751-019-1589-4.

[7] Ryoto Iwai. *Demonstration of phase space compression for positive muon beams with a helium gas target.* Doctoral thesis, ETH Zurich, Zurich, 2022. URL https://doi.org/10.3929/ethz-b-000526116.

[8] Courtesy to Ivan Solovyev.

[9] COMSOL Collaboration. Comsol multiphysics® simulation software. https://www.comsol.com/comsol-multiphysics. Consulted June 6, 2024.

[10] K.-P. Weiss et al. Iop conference series: Materials science and engineering. *IOP Conf. Ser.: Mater. Sci. Eng.*, 102:012022, 2015. doi: 10.1088/1757-899X/102/1/012022.

[11] K. Woodruff and et al. Radio frequency and dc high voltage breakdown of high pressure helium, argon, and xenon. *Journal of Instrumentation*, 15(04):P04022–P04022, April 2020. ISSN 1748-0221. doi: 10.1088/1748-0221/15/04/p04022. URL http://dx.doi.org/10.1088/1748-0221/15/04/P04022.

[12] J. M. Somerville. Sparking potentials in a transverse magnetic field. *Proc. Phys. Soc. B*, 65: 620–629, 1952. doi: 10.1088/0370-1301/65/8/312. URL https://iopscience.iop.org/article/10.1088/0370-1301/65/8/312.

[13] MG Chemicals. 844ar-l super shield conductive coating: Technical data sheet, n.d. URL https://mgchemicals.com/downloads/tds/tds-844ar-l.pdf.

[14] Henkel AG  Co. KGaA. Stycast 2850ft with hardener catalyst 24lv, n.d. URL https://www.cryoandmore.de/web-shop/.

[15] Geant4 Collaboration. Geant4: A toolkit for the simulation of the passage of particles through matter. https://geant4.web.cern.ch/. Accessed: January 14, 2025.

[16] J. Zhang, D. Goeldi, R. Iwai, M. Sakurai, and A. Soter. Scintillation detectors with silicon photomultiplier readout in a dilution refrigerator at temperatures down to 0.2 k. *Journal of Instrumentation*, 17(06):P06024, jun 2022. doi: 10.1088/1748-0221/17/06/P06024. URL https://dx.doi.org/10.1088/1748-0221/17/06/P06024.

[17] Domenico Nero. Detectors for the hypermu and mucool experiments. *Master Thesis*, 2025.

[18] *DT-670 silicon diode.* Lake Shore Cryotronics, 10 2024. URL https://www.lakeshore.com/home.